Electronic Supporting Information for

Quinone-Annulated Imidazolium Salts as Dual Electrolyte-Sorbents for Electrochemical Capture of Carbon Dioxide

Haley A. Petersen,[1,2] Hunter J. Koltunski,[1,2] Phuc H. Pham,[1,2] Quinn M. Brink,[1,2] Ashley M. Ley,[1] Jonathan Lee,[1,2] Oliver M. Wright,[1,2] Keenan Wyatt,[1] Richard D. Noble,[1] Abdulaziz W. Alherz,[3]* Oana R. Luca[1,2]*

[1]Department of Chemistry, University of Colorado Boulder, Boulder, Colorado 80309, United States

[2]Renewable and Sustainable Energy Institute and Materials Science and Engineering Program, University of Colorado Boulder, Boulder, Colorado 80309, United States

[3]Department of Chemical Engineering, College of Engineering and Petroleum, Kuwait University, Safat 13060, Kuwait

Contents

General methods S1

2,3-dichloronaphthoquinone, hydrazine hydrate, 1-bromobutane, phthalimide, iodomethane, potassium carbonate, 1,8-Diazabicyclo[5.4.0]undec-7-ene (DBU), trifluorotoluene, mesitylene, and lithium bis(trifluormethylsulfonyl)imide (LiTFSI) were purchased from commercial sources and used as received. Potassium phthalimide was prepared through deprotonation of phthalimide in ethanol by potassium hydroxide and was filtered and dried on high vacuum prior to use. Tetrabutylammonium hexafluorophosphate (NBu_4PF_6) was recrystallized from minimal hot methanol and dried overnight on high vacuum prior to use. Acetonitrile (MeCN) was distilled and stored overnight over 4 Å molecular sieves prior to use. Deuterated acetonitrile (CD_3CN) was stored overnight over 4 Å molecular sieves prior to use.

Specialty gas cylinders for electrochemical testing were obtained from AirGas for 5% and 30% CO_2 in both N_2 and Ar. Analytical gas standards used for gas meter calibration were obtained commercially from Sigma Aldrich: Scott Gas/Air Liquide Lecture Bottles SG-2005-02875 (0.5 mol% H_2, 0.5 mol% CO, 0.5 mol% CO_2, 0.5 mol% O_2 in N_2), and SG-2004-01700 (15 mol% CO_2, 7% CO, 5% O_2 in N_2).

NMR spectra were collected using a Bruker Avance-III 300 MHz NMR Spectrometer. ^{1}H and ^{13}C spectra were referenced to the solvent residual. ^{19}F spectra were referenced to trifluorotoluene internal standard. Quantitative ^{19}F and ^{1}H NMR spectra were collected with an increased relaxation delay time of D1 = 25 s.

High-resolution mass spectrometry (HRMS) data was conducted using a Waters Synapt G2 quadrupole time of flight (q-TOF) hybrid mass spectrometer (University of Colorado Boulder Central Analytical Laboratory and Mass Spec Facility). Samples were ionized via electrospray ionization (ESI) and analyzed in positive ion mode.

All experiments included in this manuscript were performed at an elevation of 5,430 ft above sea level in Boulder Colorado.

Electrochemical methods S2

All electrochemical experiments were conducted in MeCN which had been previously distilled and stored over 4 Å molecular sieves. Cyclic voltammograms were collected on a BioLogic SP-150 potentiostat

using a 3 mm glassy carbon working electrode, Pt wire counter electrode, and single-junction silver wire pseudoreference electrode referenced externally to the ferrocene/ferrocenium couple. All solutions use 0.1 M NBu_4PF_6 supporting electrolyte unless otherwise noted. A bubbler vial was used to saturate inlet gas (Ar or CO_2) with MeCN vapor before being used to sparge the solution to minimize evaporation. The working electrode (WE) was rinsed with MeCN and gently wiped dry with a KimWipe between each scan. Solution resistance was not compensated.

Controlled current electrolysis was performed on sorbents 1, 4, 5, and 6 to observe how redox changes would impact the ionic conductivity of each species. Controlled current electrolysis was performed using a BioLogic SP-150 potentiostat using a glassy carbon working electrode, carbon cloth counter electrode, , and a single-junction silver wire pseudoreference electrode referenced externally to the ferrocene/ferrocenium couple. All solutions used 0.1 M sorbent concentration in the absence of supporting electrolyte except for sorbent **5** which was ran at 0.02 M concentration. Electrolyses were ran at -24 mA until 60 coulombs were passed.

CO_2 binding analyses were performed using special order gas mixes from AirGas of 5% and 30% CO_2 in N_2. Calculation of the dissolved CO_2 concentration in solution was performed as described as previously published.[1] $E_{1/2}$ values for the irreversible second reduction feature of each quinone under CO_2 were approximated using the inflection points of the curves. [1] $E_{1/2}$ values for the irreversible second reduction feature of each quinone under CO_2 were approximated using the inflection points of the curves. [1] CO_2 binding stoichiometry was determined by fitting the resulting plots with both n = 1 (1 CO_2 bound per doubly reduced sorbent molecule) and n = 2 (2 CO_2 bound) and accepting the fit with the higher R^2 value.[1]

Synthesis S3

Synthesis of compound 2. 1-butyl-1H-naphtho[2,3-d]imidazole-4,9-dione was synthesized over four steps following literature procedure as summarized by Figure S3.1.[2-3] The final synthetic step for the synthesis of **2** was modified from Yuan et. al[4] with 1-bromobutane rather than 1-iodobutane to acquire the bromide salt of the product. 254.289 mg (1.04 mmol) of 1-butyl-1H-naphtho[2,3-d]imidazole-4,9-dione were suspended in 5.57 mL (50 equiv) 1-bromobutane in a heavy-walled Schlenk tube. The mixture was heated overnight at 100 °C with stirring. The solution was cooled to room temperature, dried by rotary evaporation, and triturated with ethyl acetate. The product was isolated as a yellow solid (16.54 mg, 4% across 6 steps). ^{1}H NMR (300 MHz, $CDCl_3$): δ 11.82 (s, 1H), 8.25 (s, 2H), 8.08 – 7.68 (m, 2H), 4.88 (s, 4H), 2.03 (ddt, *J* = 9.2, 7.6, 3.7 Hz, 4H), 1.50 (h, *J* = 7.4 Hz, 4H), 1.02 (t, *J* = 7.4 Hz, 6H). HRMS (ESI+): m/z = 311.1769; theoretical for M+: 311.1760.

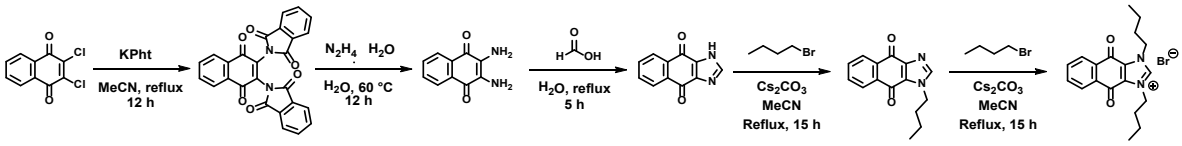

Figure S3.1. Synthetic scheme for compound **2**.

1,2-dibutyl-3-methyl-4,9-dioxo-4,9-dihydro-1*H*-naphtho[2,3-*d*]imidazol-3-ium iodide (4). The intermediate 2-butyl-1H-naphtho[2,3-d]imidazole-4,9-dione (**4a**) was first synthesized following literature procedure.[5] 399.86 mg of **4a** (1.6 mmol) were dissolved in 5 mL acetone and transferred to a heavy-walled Schlenk tube. To the mixture were added 1-bromobutane (0.45 mL, 4.2 mmol) and K_2CO_3 (654.81 mg, 4.7 mmol), and the solution was sparged with Ar for 15 minutes before sealing. The reaction was heated with stirring in an aluminum block at 100 °C for 18 h with periodic monitoring by TLC. The mixture was cooled to room temperature, vacuum filtered to remove insoluble salts, and concentrated in vacuo to yield a yellow-brown oil which was used without further purification. The crude oil was taken up in 1.0 mL acetone,

transferred to a pressure tube, and sparged with Ar for 15 minutes. The flask was charged with 1.0 mL of iodomethane (3.09 mmol), sealed, and heated with stirring at 75 °C for 22 h. The solution was concentrated under reduced pressure and dried on high vacuum, yielding the product as a dark red solid (690.46 mg, 97% yield over two steps). ^{1}H NMR (300 MHz, $CDCl_3$) δ 8.24 – 7.91 (m, 2H), 7.73 (ddd, *J* = 5.8, 4.0, 2.2 Hz, 2H), 4.41 (tt, *J* = 7.0, 3.1 Hz, 2H), 4.12 (dd, *J* = 5.4, 2.4 Hz, 3H), 3.24 – 2.93 (m, 2H), 1.93 – 1.72 (m, 2H), 1.72 – 1.54 (m, 2H), 1.52 – 1.25 (m, 4H), 0.86 (qt, *J* = 7.2, 3.0 Hz, 6H). ^{1}H NMR (300 MHz, CD_3CN) δ 8.27 – 8.15 (m, 2H), 7.97 – 7.88 (m, 2H), 4.60 – 4.49 (m, 2H), 4.13 (s, 4H), 1.89 – 1.73 (m, 2H), 1.73 – 1.60 (m, 2H), 1.57 – 1.40 (m, 4H), 0.97 (td, *J* = 7.3, 2.3 Hz, 6H).^{13}C NMR (75 MHz, $CDCl_3$) δ 175.02, 174.73, 155.19, 135.24, 131.83, 131.06, 130.06, 127.59, 127.57, 48.55, 35.71, 32.01, 29.34, 25.85, 22.85, 20.08, 13.59, 13.49. HRMS (ESI+): m/z = 325.1921; theoretical for M+: m/z = 325.1916.

Large scale synthesis of (4). Compound **4a** (5.08 g, 20 mmol) was dissolved in acetone (40 mL) and transferred to a 150 mL thick-walled pressure flask. To this solution, 1-bromobutane (4.11 g, 30 mmol) and powdered anhydrous K_2CO_3 (4.14 g, 30 mmol) were added. The flask was tightly sealed and heated in an oil bath at 100 ºC for 18 hours. After completion of the reaction, the mixture was cooled to room temperature, diluted with acetone (30 mL), and filtered through a pad of Celite to remove inorganic salts. The filter cake and reaction flask was rinsed with an additional 100 mL of acetone. The combined filtrates were concentrated under reduced pressure to afford a brown oily residue, which was used in the next step without further purification. The crude residue was re-dissolved in acetone (50 mL) and transferred to a 150 mL thick-walled pressure flask. The solution was degassed by bubbling Ar through the mixture for 15 minutes, followed by the addition of iodomethane (2.50 mL, 40 mmol) via syringe. The flask was tightly sealed and heated at 75 ºC with stirring overnight. After cooling to room temperature, the dark red solid product (7.26 g, 80% over two steps) was collected by filtration, washed with acetone, and dried on high vacuum at 45 ºC. The identity and purity of the product were confirmed by ^{1}H NMR.

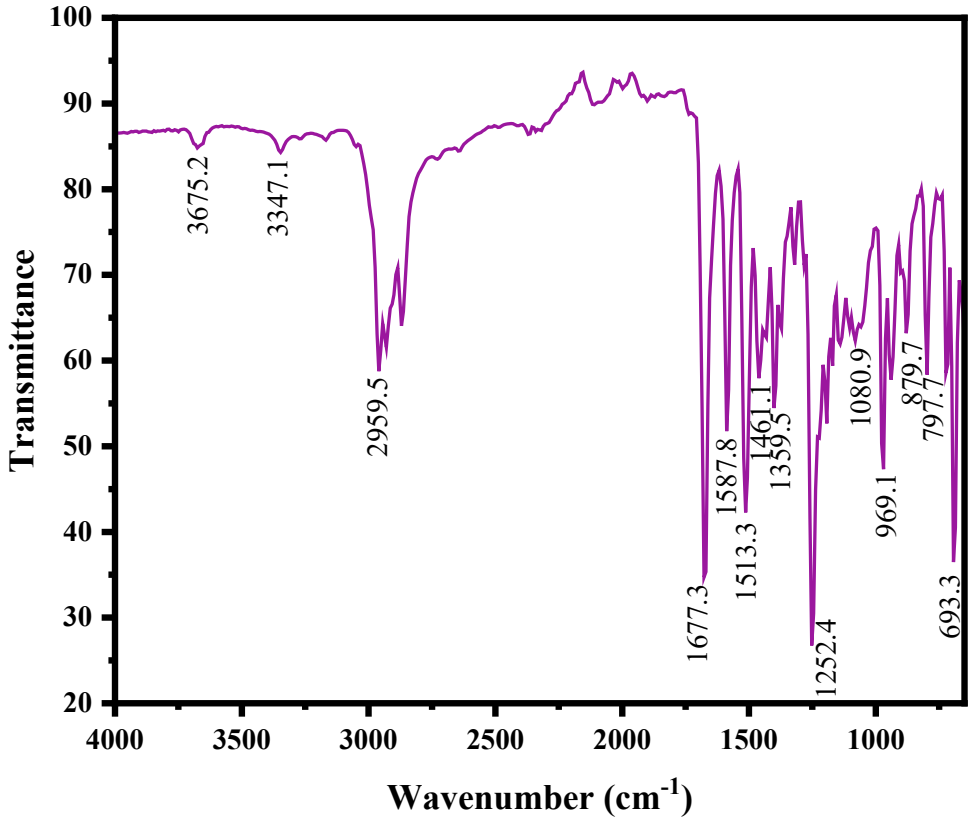

Figure S3.2. FTIR of compound **4**.

2-butyl-1,3-dimethyl-4,9-dioxo-4,9-dihydro-1*H*-naphtho[2,3-*d*]imidazol-3-ium iodide (5). 149.30 mg of **4a** (0.6 mmol) were dissolved in 5 mL acetone in a heavy-walled Schlenk tube and sparged with Ar. To the solution was added 0.13 mL (0.88 mmol) of 1,8-diazabicyclo(5.4.0)undec-7-ene (DBU), which immediately resulted in a color change from yellow to bright red. An excess of iodomethane (0.3 mL, 4.9 mmol) was added under positive pressure of Ar, and the tube was sealed. The reaction vessel was heated to 75 °C with stirring until further precipitation of red product was no longer observed (40 h). The suspension was cooled to room temperature, and the dusty red precipitate was collected by vacuum filtration and washed with additional acetone. The resulting product was dried on high vacuum, yielding 240.31 mg

(quant.). ^{1}H NMR (300 MHz, $CDCl_3$) δ 8.23 (dd, *J* = 5.7, 3.4 Hz, 2H), 7.87 (dd, *J* = 5.7, 3.3 Hz, 2H), 4.30 (s, 7H), 3.45 – 3.33 (m, 2H), 1.68 (q, *J* = 8.0 Hz, 2H), 1.60 – 1.47 (m, 4H), 1.03 (t, *J* = 7.2 Hz, 4H). ^{1}H NMR (300 MHz, DMSO) δ 8.20 (dd, *J* = 5.7, 3.3 Hz, 2H), 8.07 – 7.95 (m, 2H), 4.20 (s, 6H), 3.34 – 3.20 (m, 2H), 1.73 – 1.57 (m, 2H), 1.54 – 1.36 (m, 2H), 0.94 (t, *J* = 7.2 Hz, 3H). ^{13}C NMR (75 MHz, DMSO) δ 174.96, 154.69, 135.35, 131.54, 130.28, 126.89, 34.28, 27.65, 22.24, 21.63, 13.53. HRMS (ESI+) m/z = 2833.1440; theoretical for M+: m/z = 283.1447.

Large scale synthesis of (5). Compound **4a** (14.2 g, 56 mmol) was dissolved in acetone (45 mL) and the resulting solution was transferred to a 150 mL thick-walled pressure flask. To this solution, 1,8-diazabicyclo[5.4.0]undec-7-ene (DBU) (9.38 g, 61.6 mmol) was added, resulting in the immediate formation of a dark red precipitate. The mixture was cooled to 0 °C in an ice bath and sparged with Ar for 15 minutes. Under a constant flow of Ar, iodomethane (10.5 mL, 168 mmol) was added via syringe. The flask was then tightly sealed and heated in an oil bath at 75 °C overnight. The reaction was carried out in duplicate. After completion, both reaction mixtures were cooled to room temperature and combined. The resulting red solid was collected by filtration, washed thoroughly with acetone, and dried under high vacuum at 45 °C to afford the iodide salt product (33.4 g, 72% yield based on 112 mmol of **4a**). The identity and purity of the product were confirmed by ^{1}H NMR.

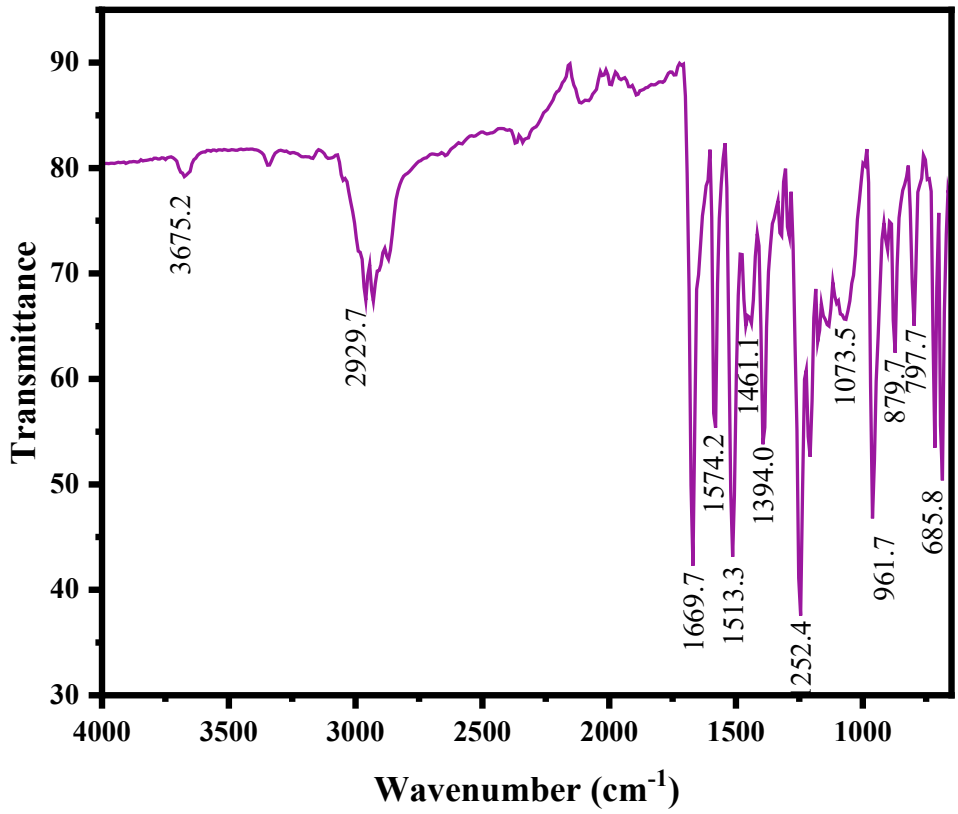

Figure S3.3. FTIR of compound **5**.

2-butyl-1,3-dimethyl-4,9-dioxo-4,9-dihydro-1*H*-naphtho[2,3-*d*]imidazol-3-ium bis(trifluoromethylsulfonyl)imide (6). In a small round-bottom flask, 199.00 mg lithium bis(trifluoromethylsulfonyl)imide (LiTFSI) and 163.77 mg of **5** were dissolved in minimal MeCN (approx. 30 mL) with stirring. 150 mL deionized water was added to the flask, resulting in a rapid solution color change from red to yellow accompanied by precipitation of a pale yellow solid. The precipitate was collected by vacuum filtration and washed with excess water. The solids were dried overnight on high vacuum at 40 °C, yielding 120.86 mg of product (54%). Completion of the ion exchange was verified with quantitative ^{19}F NMR. ^{1}H NMR (300 MHz, CD_3CN) δ 8.29 – 8.17 (m, 1H), 8.02 – 7.88 (m, 1H), 4.17 (s, 3H), 3.20 – 3.06 (m, 1H), 1.77 – 1.59 (m, 1H), 1.59 – 1.42 (m, 1H), 0.99 (t, J = 7.2 Hz, 2H). ^{13}C NMR (75

MHz, CD_3CN) δ 176.23, 136.41, 132.75, 128.14, 35.24, 28.63, 23.68, 22.98, 13.78. ^{19}F NMR (282 MHz, CD_3CN) δ -80.73.

Large scale synthesis of (6). To a 1-L Erlenmeyer flask, the iodide salt (**5**) (58.2 g, 142 mmol) was added along with acetonitrile (250 mL). The mixture was gently heated in a water bath at 45 °C to ensure complete dissolution of (**5**). Once dissolved, LiTFSI (62.0 g, 216 mmol) was added in a single portion with vigorous stirring, resulting in an immediate color change from dark red to bright yellow. Deionized water (approximately 450 mL) was then added dropwise via a dropping funnel, leading to the precipitation of compound (**6**) as a pale yellow solid. The product was collected by vacuum filtration, washed thoroughly with deionized water, and dried in a 60 °C oven for 48 hours, followed by drying under high vacuum at 50 °C for an additional 24 hours to give compound (**6**) as a yellow solid (77.8 g, 97% yield). The purity of the product was confirmed by ^{1}H and ^{19}F NMR.

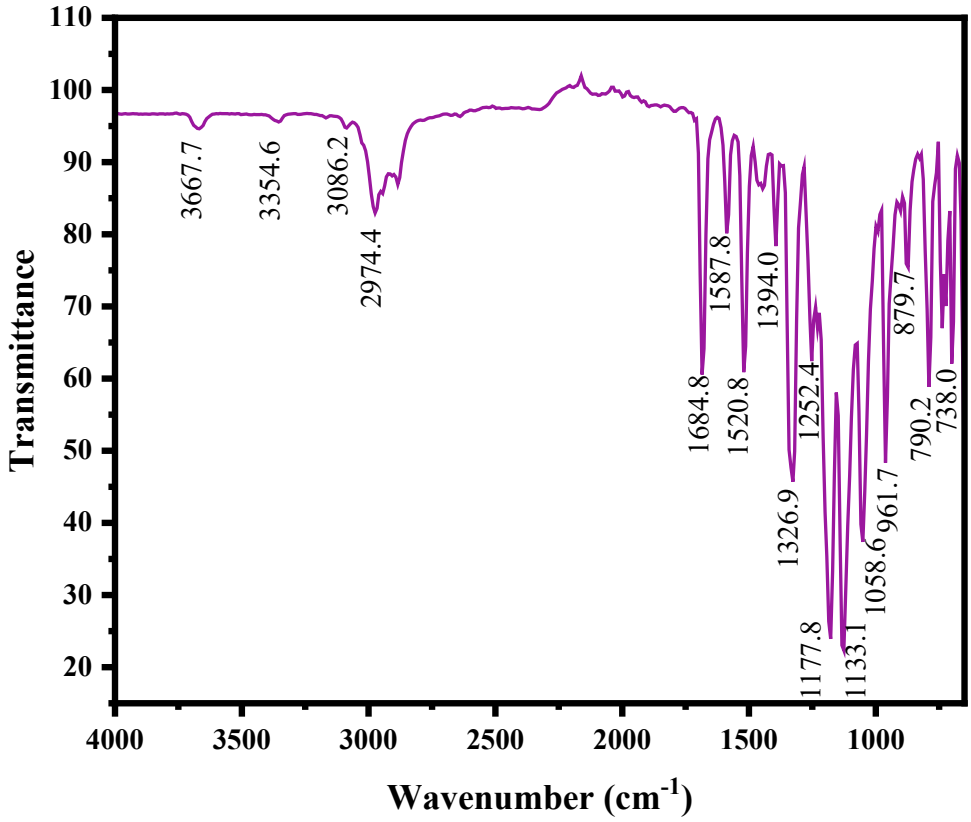

Figure S3.4. FTIR of compound **6**.

Verification of ion exchange with ^{19}F NMR S4

For each batch of TFSI salt (**6**) synthesized, a solution of analyte with trifluorotoluene internal standard was prepared by massing trifluorotoluene directly into a volumetric flask. A known mass of analyte was then added, and the components were diluted to the mark of the flask with CD_3CN. The flask was inverted several times to ensure adequate mixing. An aliquot of the solution was transferred to an NMR tube and submitted for quantitative ^{19}F NMR with D1 = 25 seconds. The resulting spectra were referenced to the

internal standard peak and integrations of the internal standard was compared to that of the TFSI signal to calculate the percent ion exchange observed.

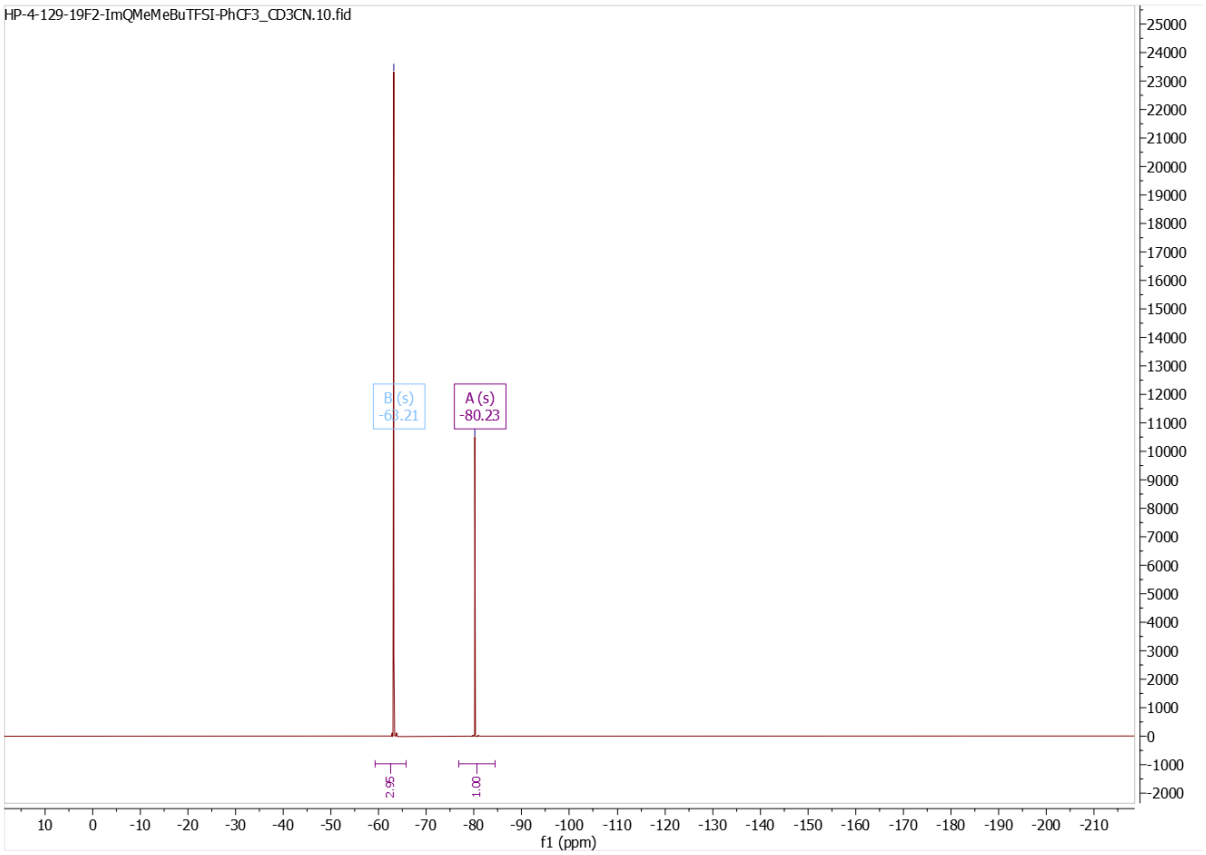

Figure S4.1. Quantitative ^{19}F NMR of **6** used to confirm quantitative ion exchange of iodide for TFSI. The internal standard peak is shown in blue, while the TFSI analyte peak is indicated in purple.

Table S4.1 ^{19}F NMR peak integration data used to verify quantitative ion exchange for compound **6**. Internal standard (IS) = trifluorotoluene. The masses noted were dissolved in CD_3CN in a 5.00 mL volumetric flask and diluted to the mark**.**

Mass (mg)	**Standard (IS)**	**Mass IS (mg)**	**IS peak (ppm)**	**IS int.**	**IS #F**	**TFSI peak (ppm)**	**TFSI int.**	**TFSI #F**	**Mol TFSI (Calc.)**	**Purity (%)**
10.86	$PhCF_3$	16.44	**-63.72**	2.95	3	**-80.74**	1.00	6	1.9E-05	99

Solubility analysis S5

A saturated solution of analyte was prepared by adding analyte to an aliquot of CD_3CN until undissolved solids remained. The solution was then sonicated in an ultrasonic bath for 30 minutes to ensure maximal dissolution of compound, followed by equilibrating at room temperature (21 °C) for 30 minutes. The solution was syringe filtered. A known mass of mesitylene internal standard was massed directly into an NMR tube. An aliquot of saturated solution was dispensed into the NMR tube containing mesitylene using an analytically calibrated Mohr pipet. The solution was mixed thoroughly by repeated inversion and submitted for ^1H NMR analysis with an increased relaxation delay time of D1 = 25 seconds.

Solubility was determined by comparing the integration of the internal standard to the integration of analyte peaks in the saturated solution.

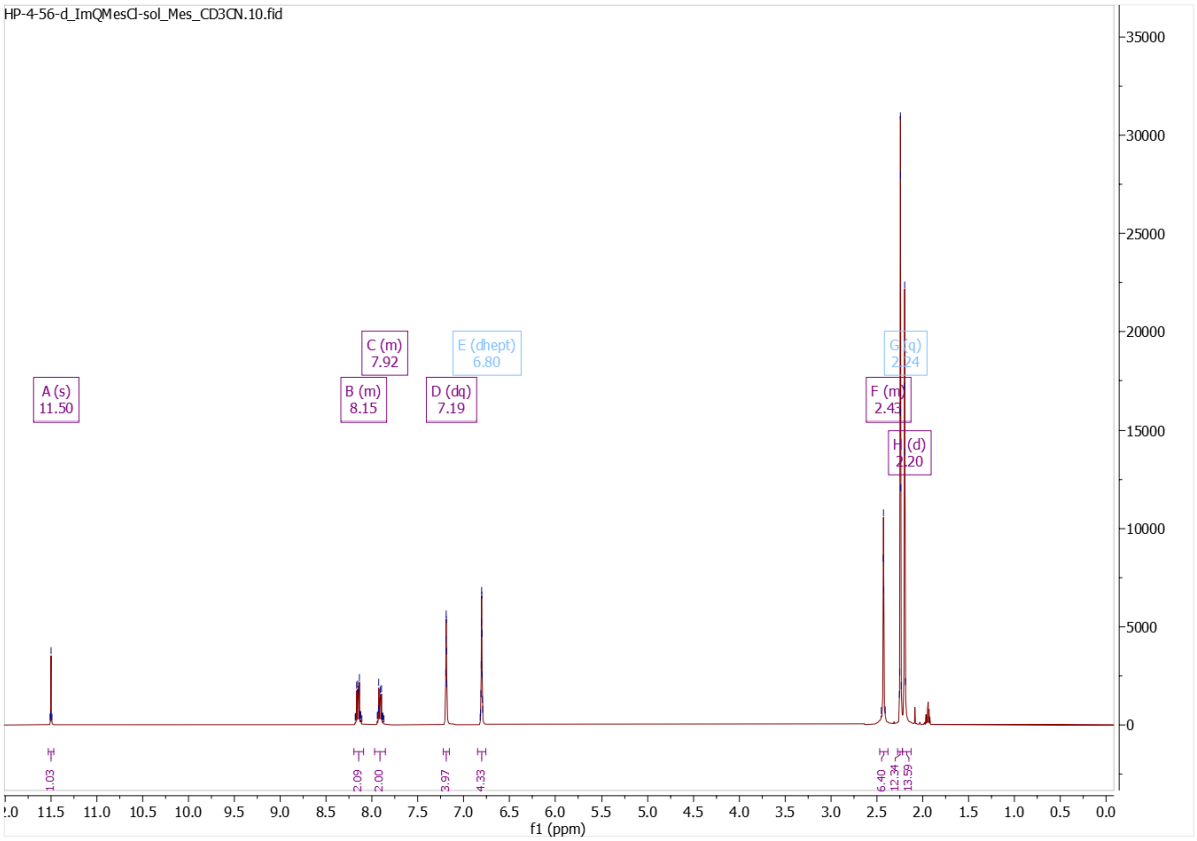

Figure S5.1. ^{1}H NMR of saturated solution of 1 (peaks labelled in purple) in CD_3CN with mesitylene internal standard (peaks labelled in blue). 11.02 mg mesitylene internal standard were massed into a separate tared vial. A 0.585 mL aliquot of saturated solution was dispensed into the vial containing mestiylene using an analytically calibrated Mohr pipet.

Although these structures did not achieve ionic liquid status, some of the desirable properties of ionic liquids may be achieved instead through high solubility of the compounds in the solvent of interest. With sorbents **4** – **6** in hand, we sought to establish the solubility of each new sorbent in our electrochemical solvent of choice, MeCN. Anhydrous CD_3CN was saturated with each salt, and solubility was determined by ^{1}H NMR by comparison of analyte peak integrations to those of mesitylene internal standard. The results are presented in Table S5.1.

Table S5.1. Solubilities of sorbents **4** – **6** in anhydrous acetonitrile at room temperature (21 °C).

Sorbent	**Solubility in anhydrous CD_3CN, 21 °C (M)**
4	0.16
5	0.02
6	2.87

Although **6** remains a solid, the simple exchange of the iodide counterion in **5** for TFSI improved solubility by over a full order of magnitude. This is consistent with the expected ion association of the two anions; a relatively small anion is replaced by the bulky TFSI, which cannot associate as tightly with the cation.

Electrochemical characterization S6

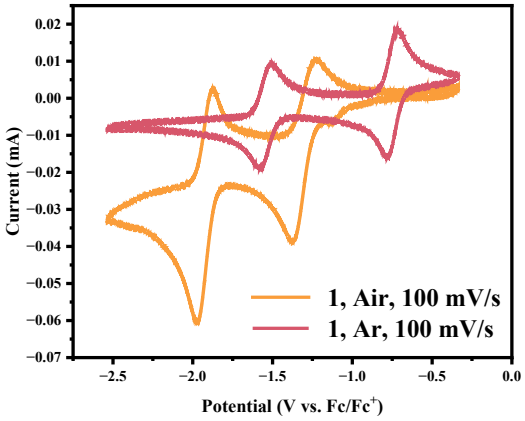

Figure S6.1. CVs of 1 mM **1** with 0.1 M NBu_4PF_6 supporting electrolyte under inert Ar atmosphere (red) and under air (orange) collected at a scan rate of 100 mV/s.

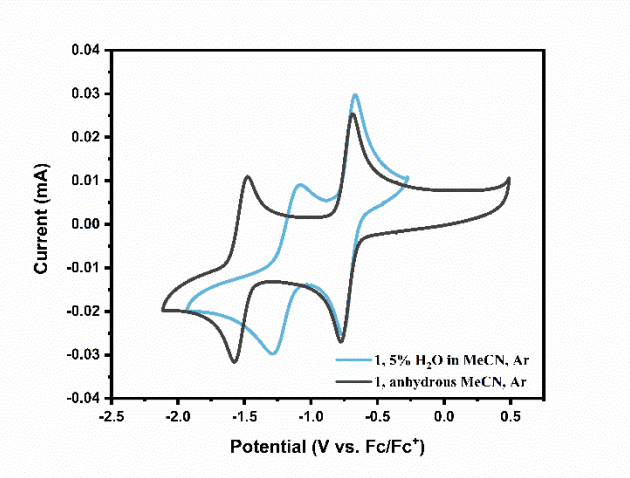

Figure S6.2. CVs of 1 mM **1** in anhydrous MeCN (blue) and in 95:5 MeCN:H_2O (red) with 0.1 M NBu_4PF_6 supporting electrolyte, collected at a scan rate of 100 mV/s.

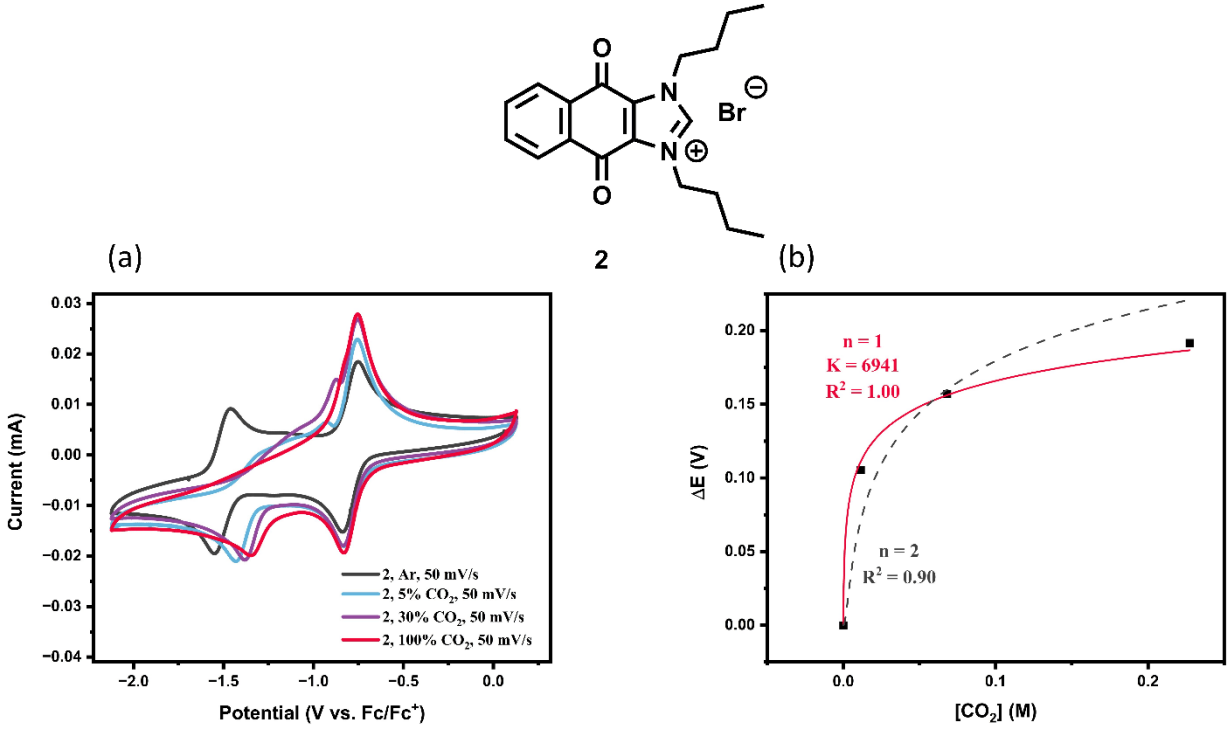

Figure S6.3. (a) 1 mM CVs of **2** under varying concentrations of CO_2 collected with a scan rate of 50 mV/s. (b) fit of $\boldsymbol{\Delta E = \frac{RT}{F} ln(K[CO_2]^n + 1)}$ to find the equilibrium constant K and stoichiometry n of CO_2 molecules binding to sorbent.

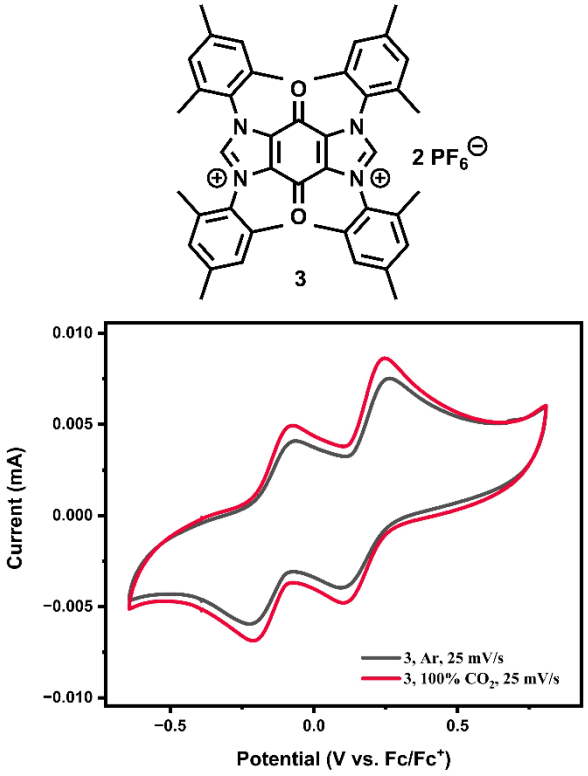

Figure S6.4. 1 mM CVs of **3** under varying concentrations of CO_2 collected with a scan rate of 25 mV/s. No shift in potential is observed.

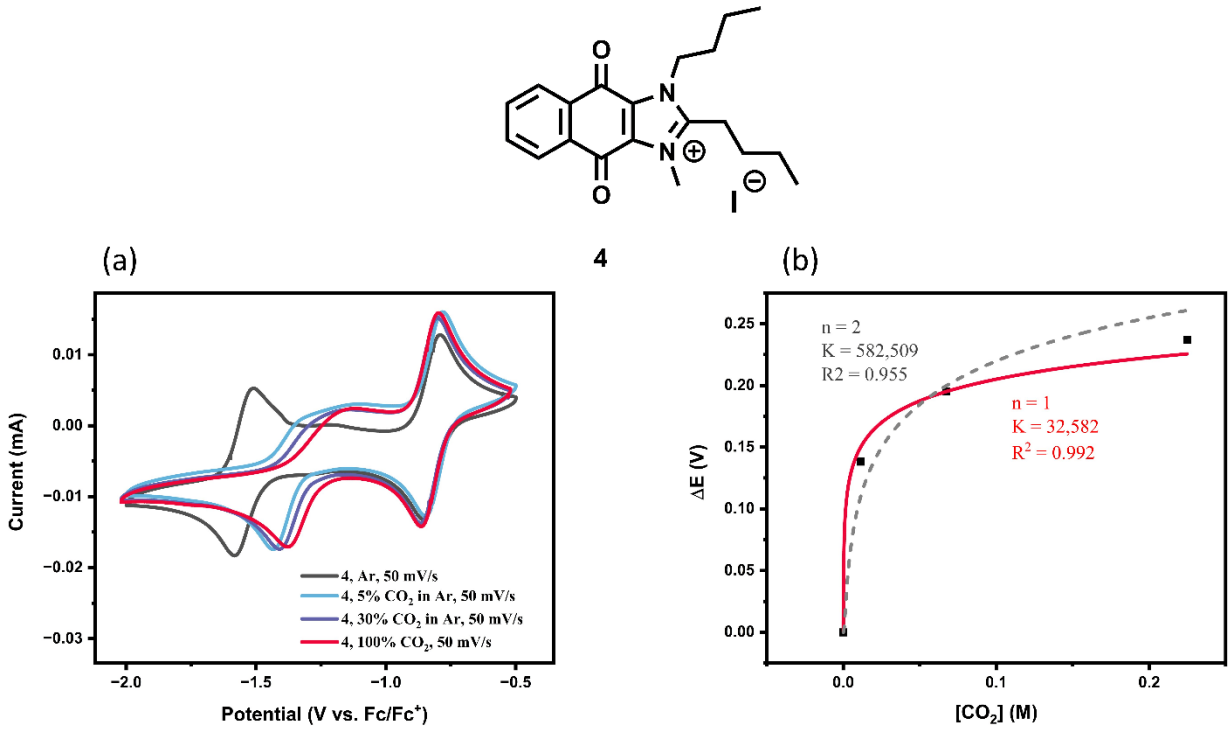

Figure S6.5. (a) 1 mM CVs of **4** under varying concentrations of CO_2 collected with a scan rate of 50 mV/s. (b) fit of $\boldsymbol{\Delta E = \frac{RT}{F} ln(K[CO_2]^n + 1)}$ to find the equilibrium constant K and stoichiometry n of CO_2 molecules binding to sorbent**.**

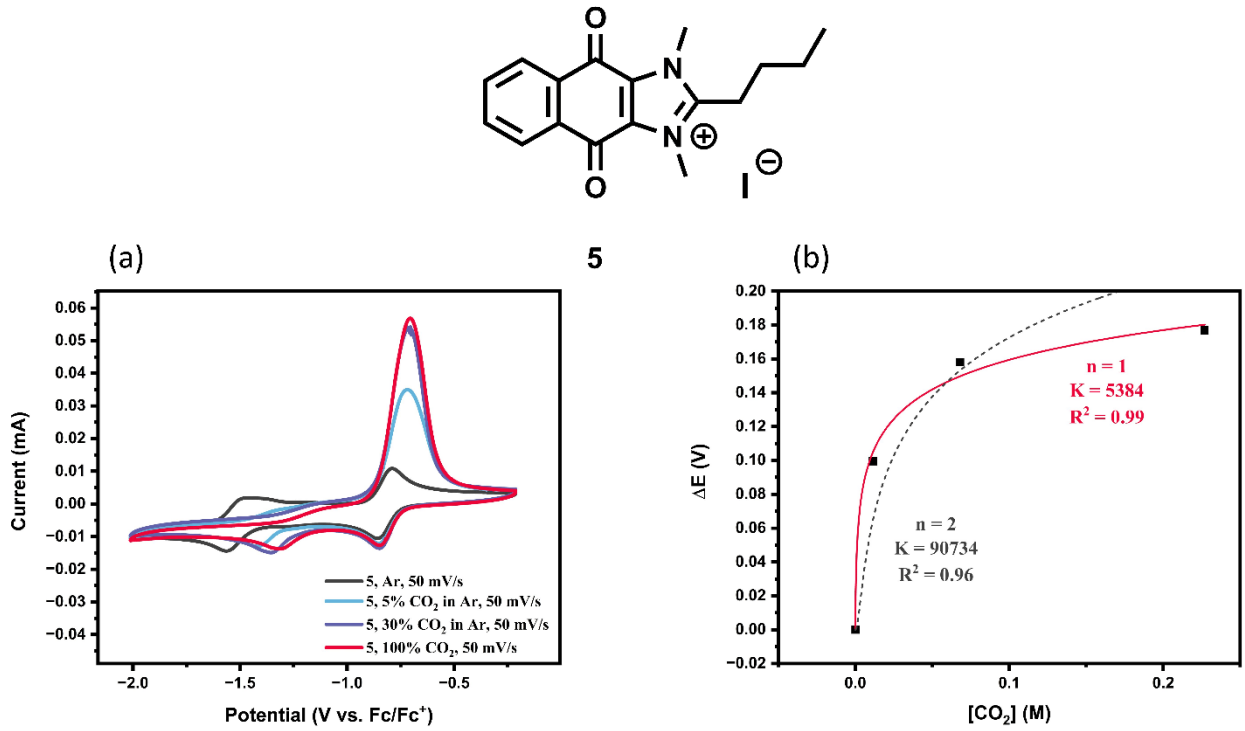

Figure S6.6. (a) 1 mM CVs of **5** under varying concentrations of CO_2 collected with a scan rate of 50 mV/s. (b) fit of $\boldsymbol{\Delta E = \frac{RT}{F} ln(K[CO_2]^n + 1)}$ to find the equilibrium constant K and stoichiometry n of CO_2 molecules binding to sorbent.

Aside from the nonstandard behavior of the adduct reoxidation for sorbents **5** and **6**, all quinones otherwise exhibit the expected features under increasing amounts of CO_2 apart from sorbent **3**. Under Ar, two reversible reductions are observed for each, assigned to the usual quinone-centered reductions. Under 5% and 30% CO_2 (blue and purple traces in each figure), a small reoxidation is observed close in potential to the second reduction feature. This is attributed to reoxidation of the doubly reduced species (without bound CO_2) to their singly reduced forms. Under 100% CO_2, these features become negligible. In each case, a new oxidation feature grows in under increasing amounts of CO_2 and reaches its maximum current at 100% CO_2. This is consistent with complete depletion of the doubly reduced species in favor of CO_2 adduct formation in the presence of high concentrations of CO_2.

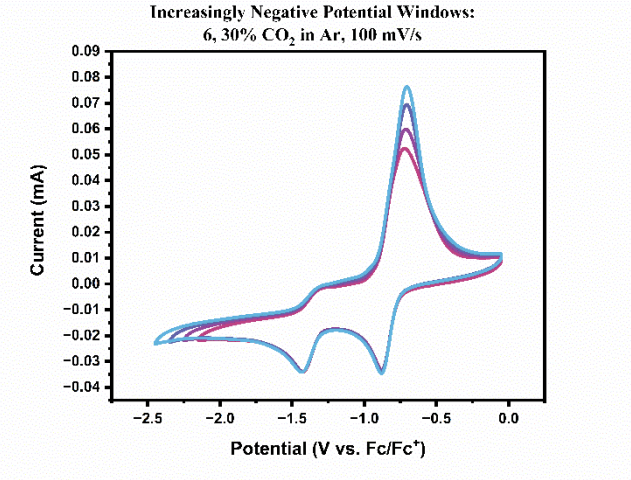

Figure S6.7. CVs of 1 mM **6** in 0.1 M NBu_4PF_6 in anhydrous MeCN taken at 50 mV/s under 30% CO_2 in Ar at successively more negative switching potentials. Growth in the oxdiation feature at -0.7 V vs. Fc/Fc^+ indicates that it is likely preceded by a chemical step.

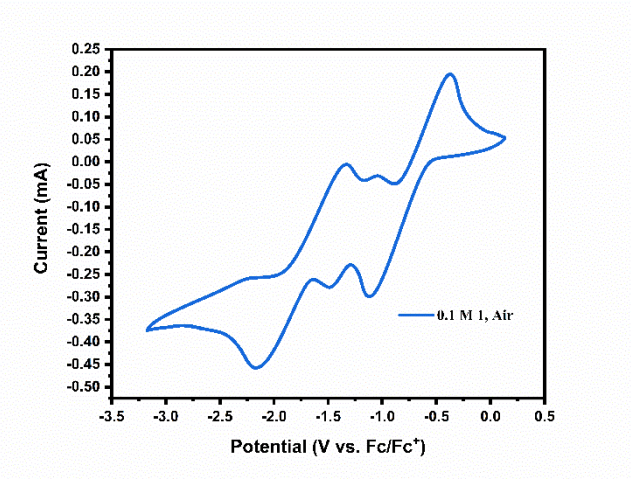

Figure S6.8. CV of 0.1 M **1** in MeCN without supporting electrolyte under ambient air collected at a scan rate of 100 mV/s.

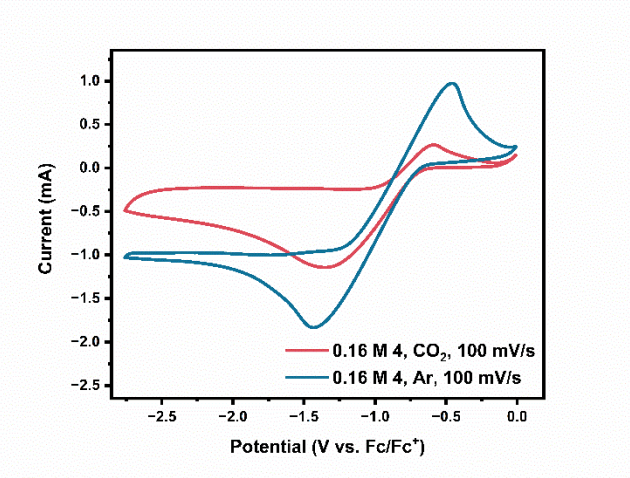

Figure S6.9. CVs of 0.16 M **4** in MeCN without added supporting electrolyte, collected at 100 mV/s.

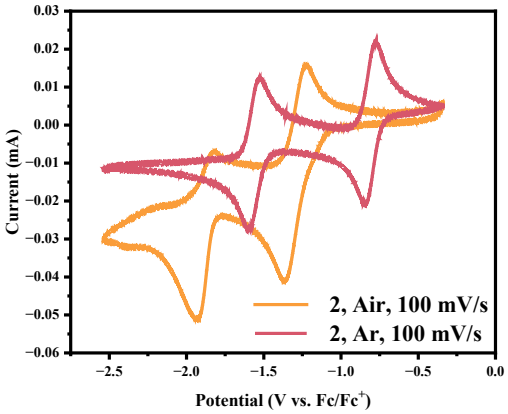

Figure S6.10. CVs of 1 mM **2** with 0.1 M NBu_4PF_6 supporting electrolyte under inert Ar atmosphere (red) and under air (orange) collected at a scan rate of 100 mV/s.

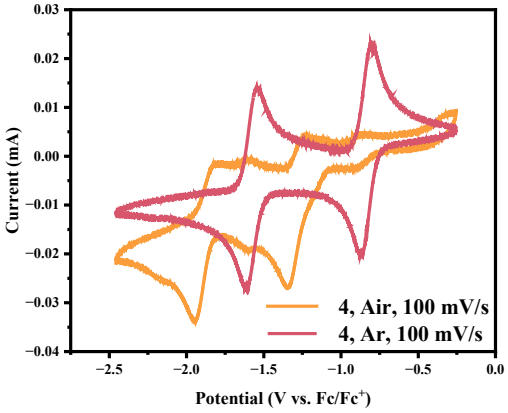

Figure S6.11. CVs of 1 mM **4** with 0.1 M NBu_4PF_6 supporting electrolyte under inert Ar atmosphere (red) and under air (orange) collected at a scan rate of 100 mV/s.

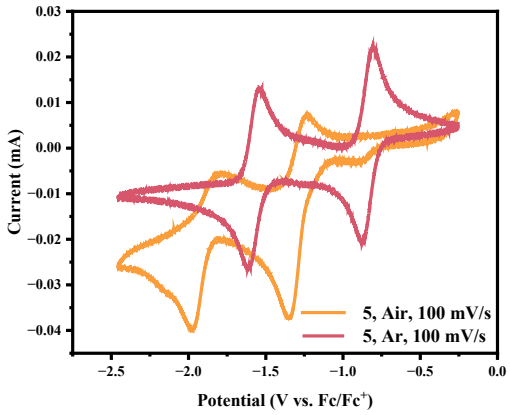

Figure S6.12. CVs of 1 mM **5** with 0.1 M NBu_4PF_6 supporting electrolyte under inert Ar atmosphere (red) and under air (orange) collected at a scan rate of 100 mV/s.

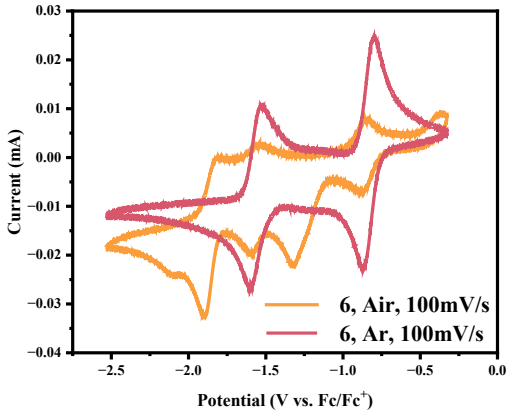

Figure S6.13. CVs of 1 mM **6** with 0.1 M NBu_4PF_6 supporting electrolyte under inert Ar atmosphere (red) and under air (orange) collected at a scan rate of 100 mV/s.

Conductivity measurements S7

Electrochemical impedance spectroscopy (EIS) was used to measure the electrolyte conductivity. The measurements were carried out using a Bio-Logic SP-300 potentiostat. A frequency sweep from 1 MHz to 1 kHz was conducted with the voltage held constant at 0 V vs Voc. The experimental setup consisted of a custom symmetric cylindrical cell, equipped with Pt as the working and counter electrode material,

configured in a two-electrode system. The electrodes had a surface area of 1 cm² and were spaced 1 cm apart.

Table S7.1. Conductivity values for the various sorbents.

Sorbent	R_{sol} (Ohm)	p (Ohm*m)	Conductivity (S/cm)
1 (0.1 M)	395	3.95	0.00253
4 (0.1 M)	213	2.13	0.00469
5 (0.1 M)	584	5.84	0.00171
6 (0.1 M)	135	1.35	0.00741
6 (0.8 M)	51	0.51	0.0196

Table S7.2. Conductivity values for various sorbents before electrolysis and after electrolysis under Ar.

Sample (0.1 M)	p (Ohm*m)	Conductivity ($S*cm^{-1}$)	Comments
1 pre-electrolysis	3.34	0.00299	
1 post-electrolysis (Ar)	3.93	0.00254	15 % decrease
4 pre-electrolysis	1.38	0.00725	
4 post-electrolysis (Ar)	1.81	0.00552	24 % decrease
5 pre-electrolysis	4.26	0.00235	
5 post-electrolysis (Ar)	5.51	0.00181	23 % decrease
6 pre-electrolysis	1.24	0.00806	
6 post-electrolysis (Ar)	1.44	0.00694	14 % decrease

Stability studies S8

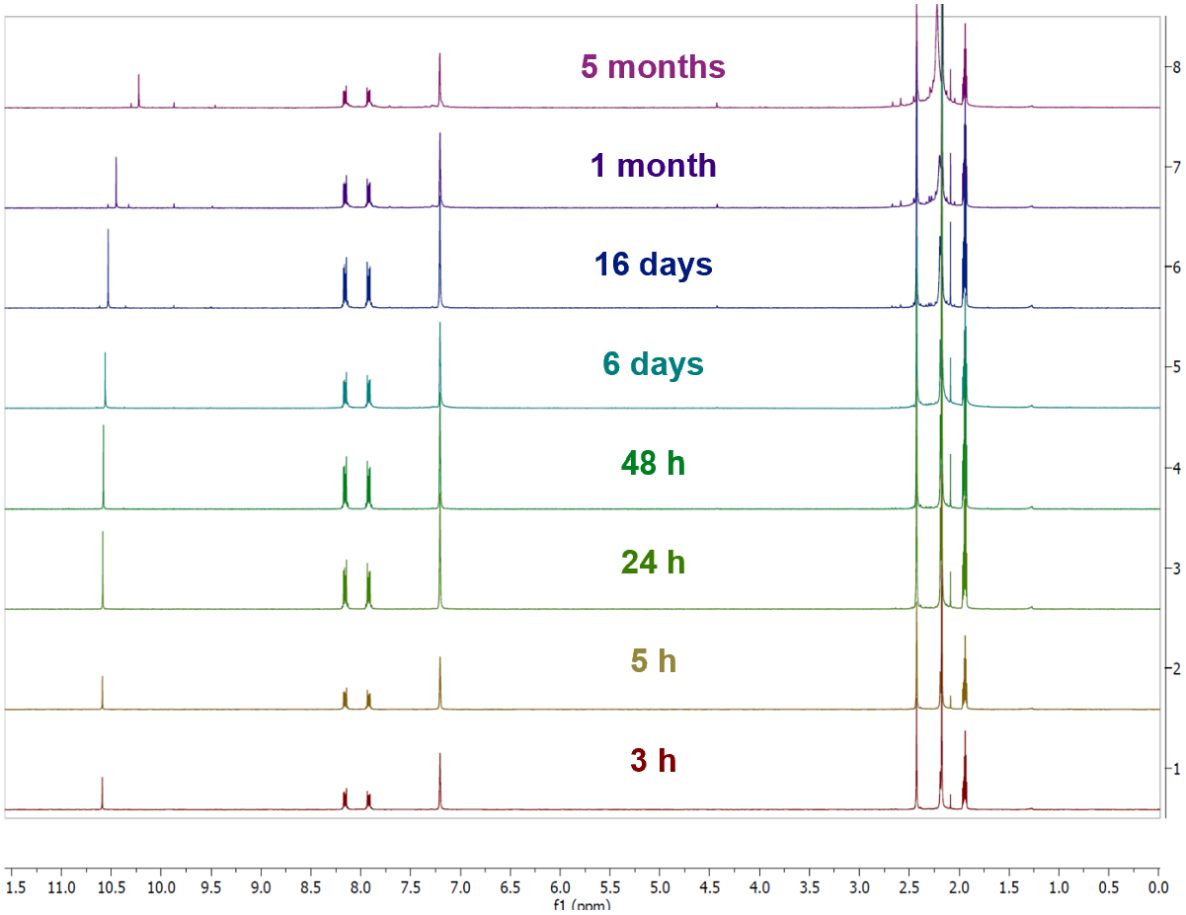

Figure S8.1. ^{1}H NMR of 10 mM **1** in CD_3CN over time. Red: 3 hours after sample preparation; yellow: 5 hours; lime green: 24 hours; dark green: 48 hours; teal: 6 days; blue: 16 days; purple: 1 month; pink: 5 months.

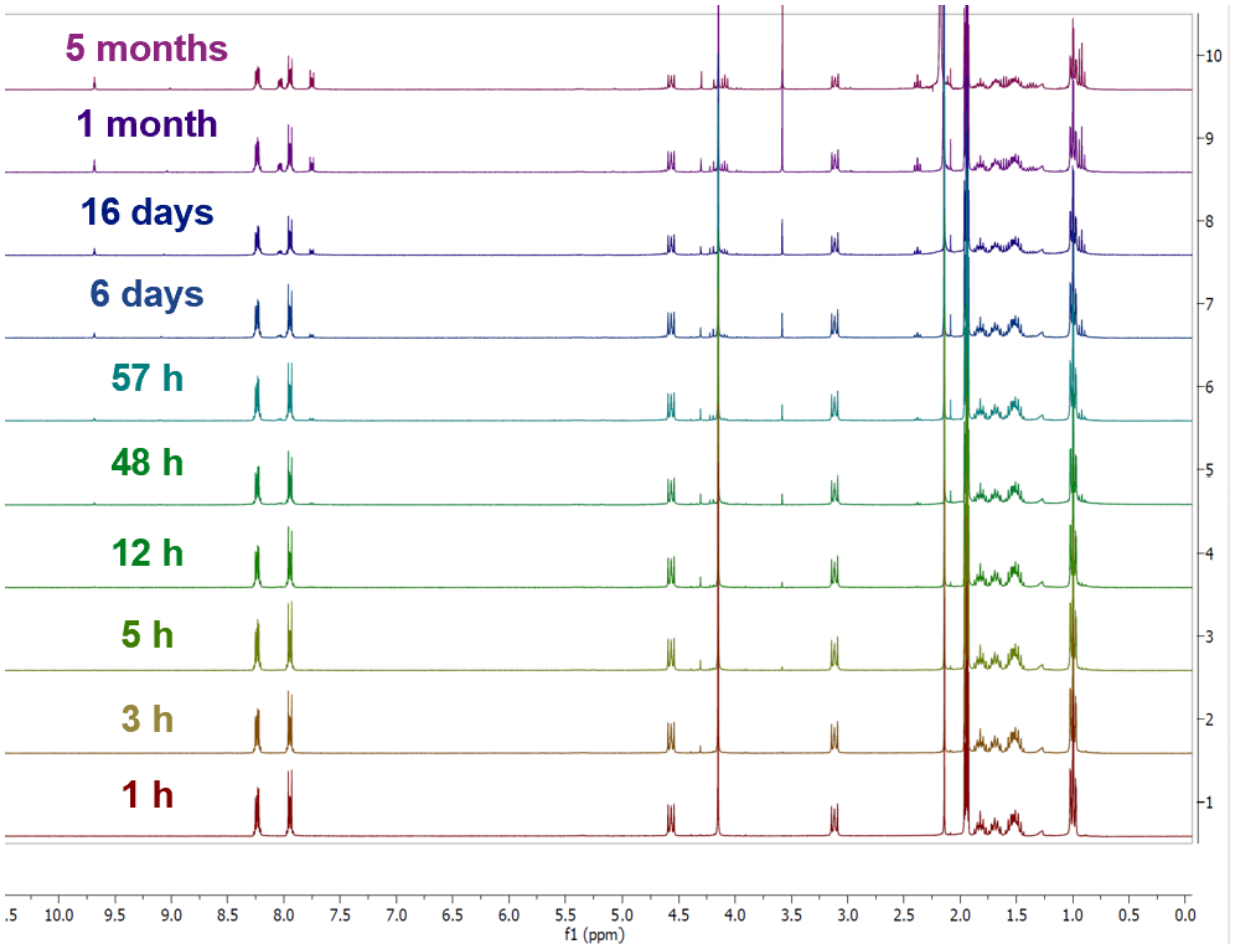

Figure S8.2. ^{1}H NMR of **4** in CD_3CN over time.

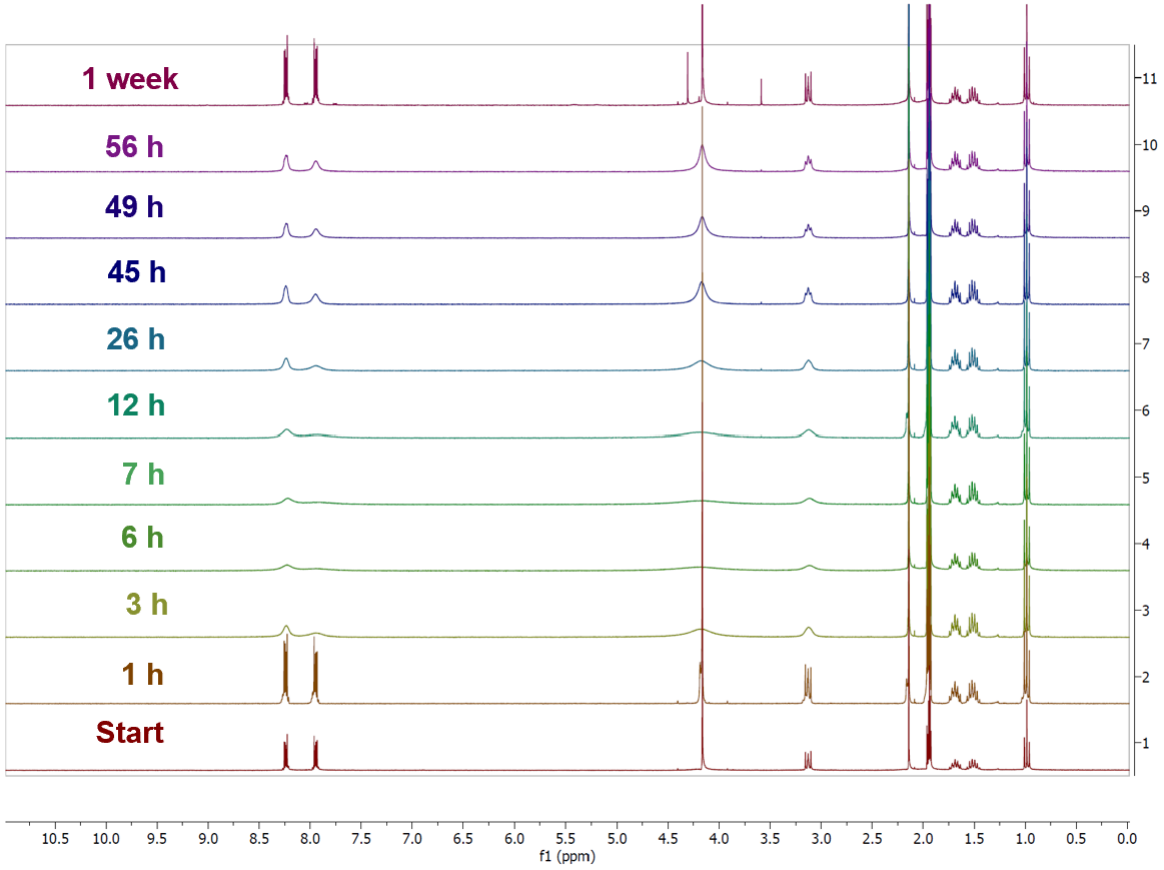

Figure S8.3. ^{1}H NMRs of **5** in CD_3CN monitored over time.

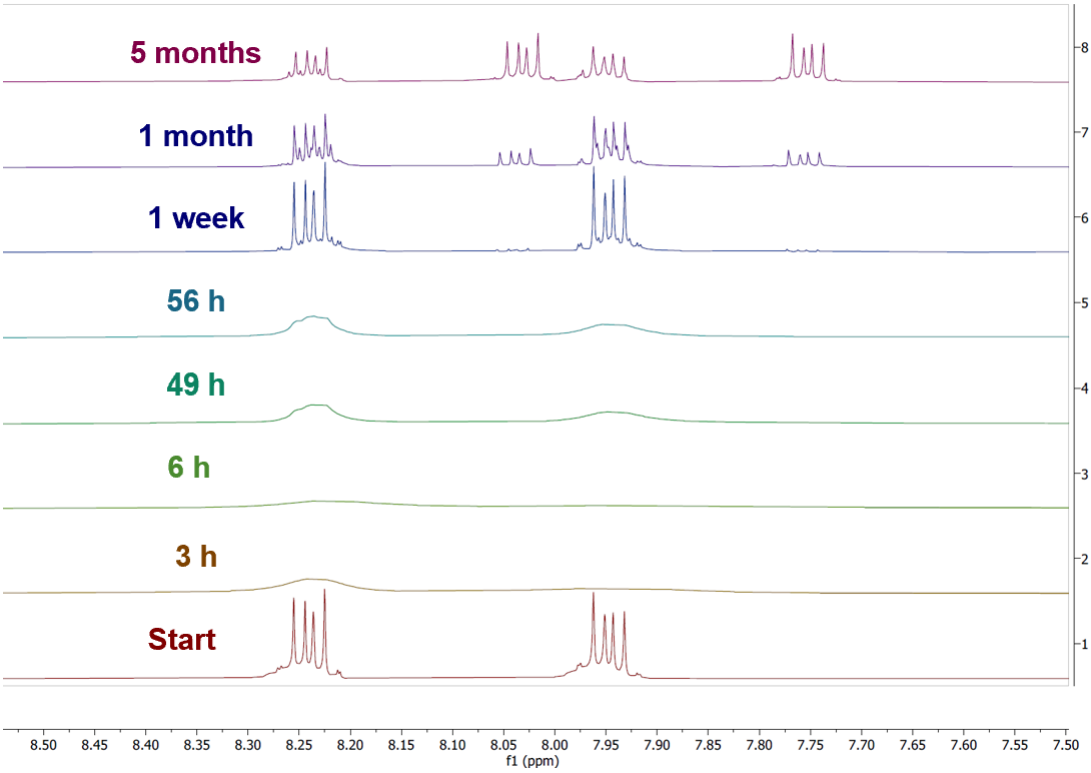

Figure S8.4. Aromatic ^{1}H NMR region for **5** over time, indicating formation of a new substance. Relative integrations of the peaks shown at 5 months suggest at least two separate naphthoquinone-based species present, with the species possessing new dd at 8.04 ppm and 7.76 ppm constituting the majority species.

The unexpected peak broadening behavior of **5** in solution is hypothesized to occur due to a radical reactivity of **5** with the iodide anion. Broadened NMR peaks are a hallmark of paramagnetism, but only certain peaks belonging to **5** are affected. The ^{1}H signals corresponding to the -$CH_2CH_2CH_3$ protons of the C2 butyl group are largely unaffected and remain sharp throughout the duration of the experiment. Based upon this observation, we propose that formation of a radical species on the central naphthoquinone ring explains selective peak broadening through the resonance forms shown in Figure S8.5. Due to the high conjugation of the naphthoquinone backbone of **5**, any radical generated on the structure is delocalized across the entire pi system, causing a perturbation in the local magnetic field for all aromatic protons as well as the close-proximity N-CH_3 and butyl CH_2 group at the point of attachment. In contrast, the

remaining three signals for the butyl group (1.68, 1.51, and 0.99 ppm) correspond to protons that are located farther away from the unpaired electron, and consequently from the magnetic field disturbance.

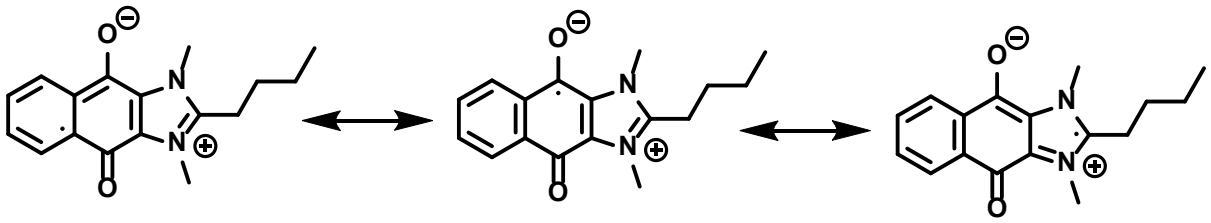

Figure S8.5. Radical resonance of singly reduced **5** invoked to explain the selective peak broadening observed in the ^{1}H NMR of **5**.

We hypothesized that such a radical species could form due to the redox reactivity of the I^- counterion. Because I^- is known to oxidize readily to ½ I_2 (alternatively, $I^{\bullet}$) in the presence of air, we hypothesized that the counterion could be responsible for promoting radical formation and subsequent degradation of the sorbent.

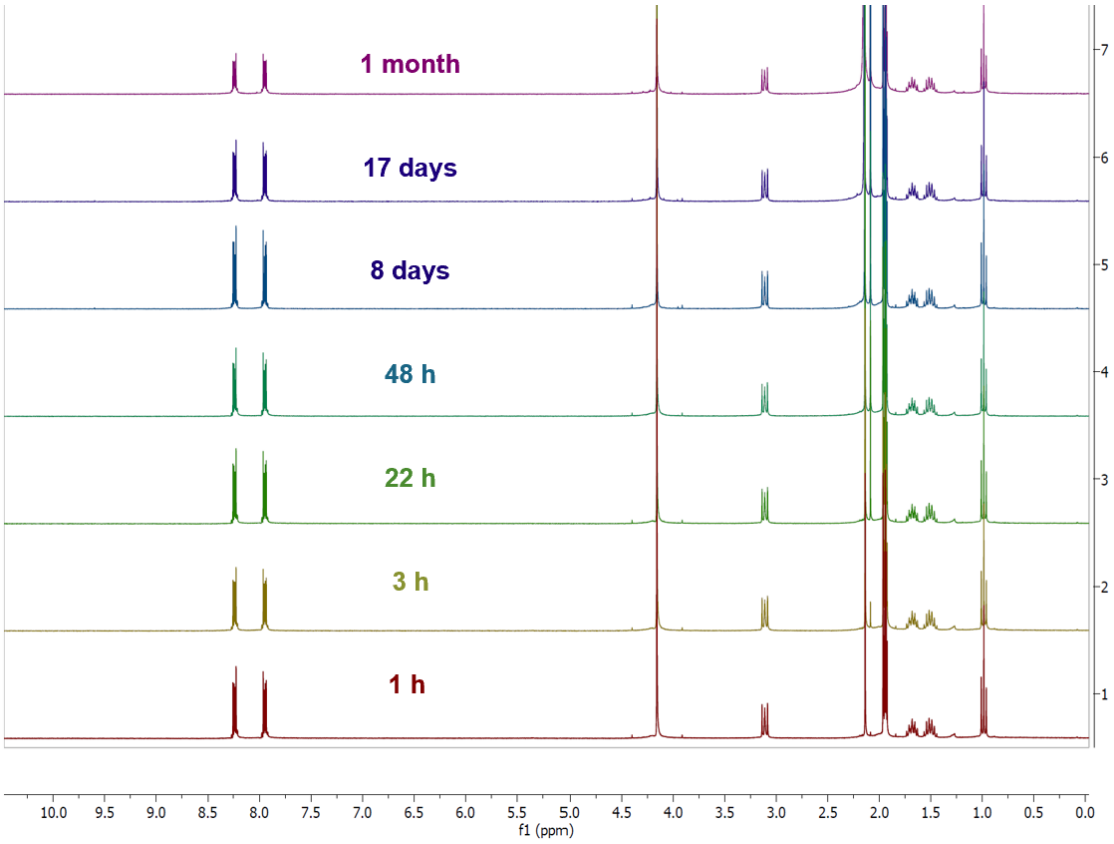

Figure S8.6. ^{1}H NMR stability studies of 10 mM **6** in CD_3CN solution over one month show no change in signals and no peak broadening comparable to that observed for **5**.

Sorbent degradation S9

X-ray crystallography. Crystals suitable for diffraction were grown by slow evaporation from a concentrated solution of **1'** in 1:1 MeCN:H_2O. Single-crystal XRD data for the structural determination of **1'** was collected, solved, and refined under the guidance of Dr. Matthias Zeller, Purdue University. Data was collected at 150 K with a Bruker AXS D8 Quest diffractometer equipped with PhotonIII_C14 charge-integrating and photon counting pixel array detector. A laterally graded multilayer (Goebel) mirror was used for wavelength selection of Cu Kα radiation (1.541178 Å) from a microsource (Iμs) X-ray tube. Data were processed using APEX 4 (Bruker).[6] The crystal under investigation was found to be non-merohedrally twinned. The orientation matrices for the two components were identified using the program Cell_Now,[7] with the two components being related by a 180 degree rotation around the real c-axis. The two components were integrated using SAINT and corrected for absorption using TWINABS.[8] The structure was solved using dual methods with the non-overlapping reflections of both components.[9] The structure was refined using the hklf 5 routine with all reflections of both components (including the overlapping ones), resulting in a BASF value of 0.364(1). One of the methyl groups was refined as disordered with a 30-degree rotation. The occupancy ratio was refined to 0.62(4) to 0.38(4). The amine hydrogen position was refined.[10-11] Table S9.1 reports key values for the crystal analyzed. For further information, see the separately attached .cif file.

Table S9.1. Experimental details for the crystallographic study of **1'**.

Formula	$C_{29}H_{28}N_2O_3$
Formula Weight	452.53
Crystal system	Monoclinic
Space Group	$P2_1/c$
a (Å)	13.6679(4)
b (Å)	20.5349(7)
c (Å)	8.6948(3)
α (°)	90
β (°)	104.799(2)
γ (°)	90
V (Å^3)	2359.41(14)
Formula units per cell (Z)	4
Crystal dimensions (mm)	0.19 x 0.09 x 0.03
μ (mm^{-1})	0.658
S	1.068
R_1, wR_2 (all reflections)	0.084, 0.1571
R_1, wR_2 ($I > 2\sigma(I)$)	0.0581, 0.1385
Reflections	8288
Parameters	318
Restraints	0

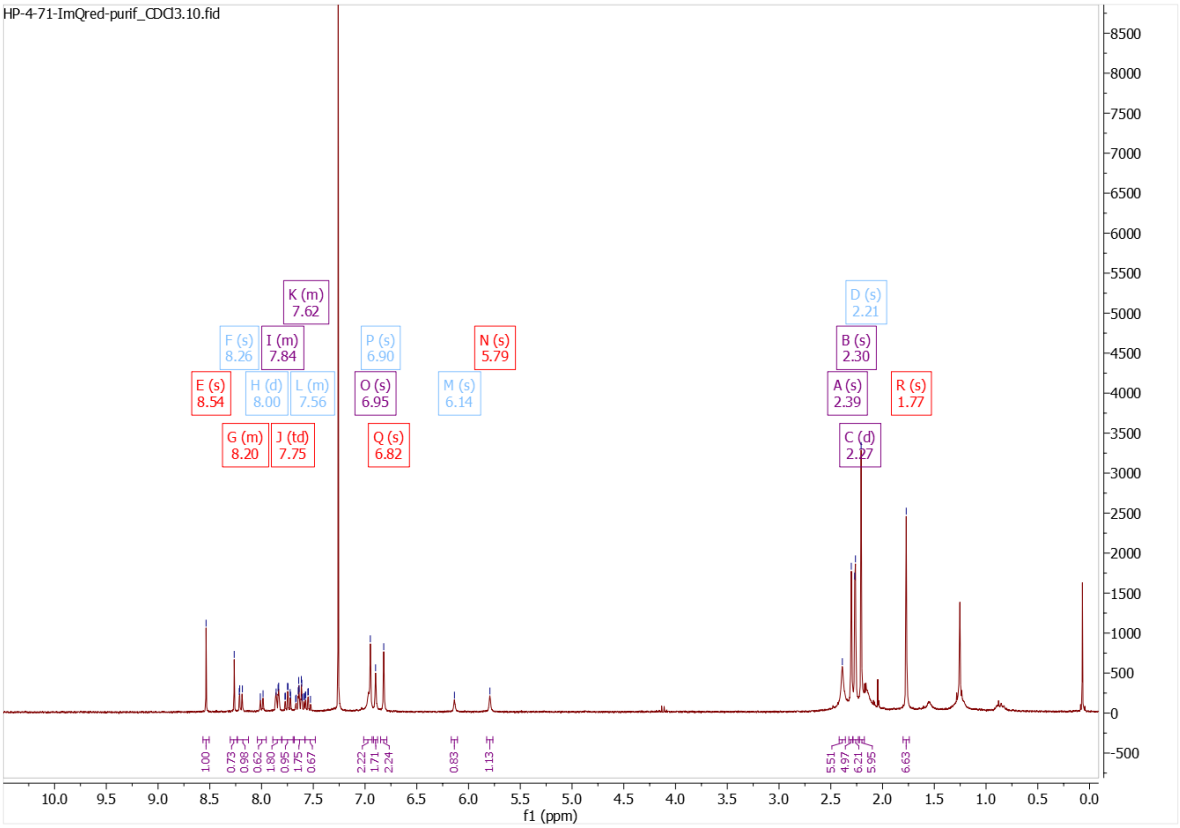

Figure S9.1. ^{1}H NMR in $CDCl_3$ of degradation product **1'**. Peaks assigned to the major rotomer are labelled in red, those assigned to the minor rotomer are labelled in blue, and peaks with overlapping signal from both rotomers are labelled in purple.

NMR assignment. The structure of **1'** as determined by single-crystal XRD reveals the expected breaking of symmetry (cleavage of the imidazolium ring of **1**) as well as a hydrogen bonding interaction between the oxygen of the amide and the adjacent N-H proton (H—acceptor distance 2.99 Å, considered medium strength).[12] This observation, combined with the steric bulk of the mesityl groups, suggests hindered rotation about the C-N bond, and thus we assign the ^{1}H NMR as a mixture of two rotamers coexisting in a 4:5 ratio. COrrelated SpectroscopY (COSY) NMR is additionally provided:

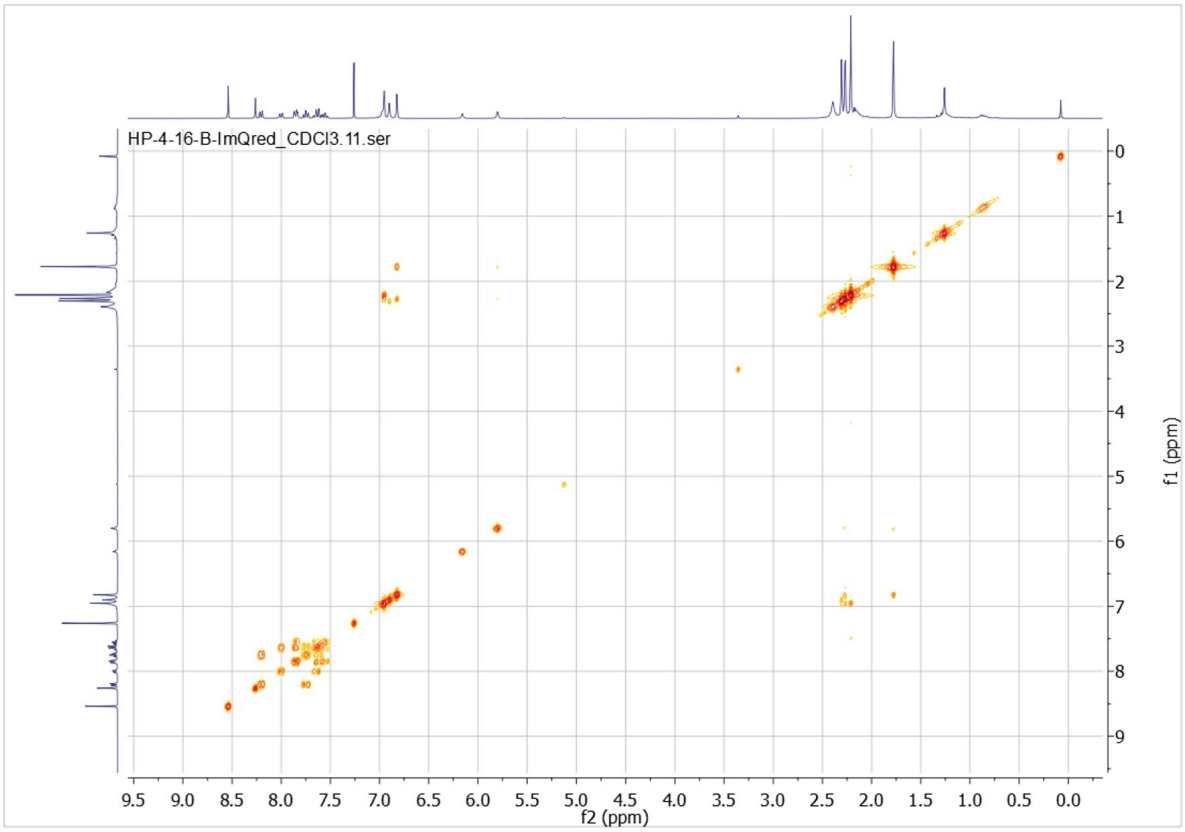

Figure S9.2. COSY NMR of compound **1'** in $CDCl_3$.

Off-diagonal peaks show clear coupling between mesityl aromatic hydrogens and their corresponding methyl hydrogens (e.g. 1.77 ppm, 6.82 ppm; 2.27 ppm, 6.82 ppm; 2.30 ppm, 6.90 ppm; 2.21 ppm, 6.95 ppm). Off-diagonal peaks in the aromatic region additionally demonstrate coupling between adjacent hydrogens of the naphthoquinone ring for each rotamer. The observed couplings were used in conjunction with analysis of observed integrations to assign peaks to the major and minor rotamer.

Computational details S10

In contrast to commercially available quinones that have been previously assessed for this application, the quinones in this study can only bind 1 CO_2 molecule per quinone, as they are relatively weaker nucleophiles.[13] Frequency calculations were conducted to confirm that the optimized geometries did not exhibit any imaginary frequencies, ensuring they correspond to true minima on the potential energy surface, and to determine thermal and entropic corrections for calculating Gibbs free energies. In order to corroborate the experimental findings of reaction stoichiometry, our calculations estimated a partial pressure of CO_2 in the presence of quinones and their reduced forms to be 1 atm, 12.25 atm, 75 atm, and 248.5 atm to simulate experimental conditions where the electrochemical reduction of quinones occurred at different Quinone:CO_2 ratios, as summarized in Table 2.

Table S10.1. Percentage CO_2 dissolved in acetonitrile and corresponding concentration ratios of the Quinone and CO_2 reactants.

%CO_2	**Quinone:CO_2 Ratio**
5%	1:12.25
30%	1:75
100%	1:248.5

Varying the partial pressures primarily affects the entropic corrections, where higher pressures lead to a lower total entropy. All the calculations were conducted using Gaussian 16.[13] Two primary properties calculated via resulting Gibbs free energies were the focus of study in this work: the free energy of CO_2

binding (ΔG_{bind}) and the reduction potentials of quinones under Ar and under varying concentrations of CO_2 (E_{red}^{Ar} and $E_{red}^{n\%CO_2}$, respectively).

An in-depth study discussing the effects of two different functionals (MN15 & ω-B97xD) and two different basis sets (6-311+G(d,p) & def2-TZVP) is presented in the SI section S10. To summarize, we use different methods to calculate each property to minimize errors relative to experiment.[14-15] The MN15 functional and triple-zeta Pople basis set with polarization and diffuse functions 6-311+G(d,p) are used to calculate reduction potential values[16-17], whereas the ω-B97xD functional and Ahlrichs triple-zeta valence basis with polarization def2-TZVP is used to calculate binding energies.[18-19] Both basis sets used are large enough to ensure appropriate treatment of all atoms in these calculations.[20-23] The acetonitrile solvent was described using the SMD model as it has been demonstrated to work exceptionally well for charged systems.[24]

Based on experimental observations, CO_2 binding occurs only after a quinone has been reduced twice.[1] The energy of CO_2 binding is calculated according to the following chemical reaction in solution:

$$Q^{2-} + CO_2 \rightarrow QCO_2{}^{2-}$$

ΔG_{bind} is calculated by taking the difference between the product and reactant Gibbs free energies:

$$\Delta G_{bind} = G_{QCO_2^{2-}} - (G_{Q^{2-}} + G_{CO_2})$$

Where $G_{QCO_2{}^{2-}}$ is the Gibbs free energy of the CO_2^- bound species, $G_{Q^{2-}}$ is the free energy of the reduced quinone, and G_{CO_2} is the free energy of solvated CO_2.

Reduction potentials are calculated according to the Nernst Equation:

$$E_{red} = -\frac{\Delta G_{red}}{nF} - E_{ref}$$

Where ΔG_{red} is the free energy difference between the reduced and neutral species, $\Delta G_{red} = G_{Q^-} - G_Q$, n is the number of electrons transferred during the reduction, F is Faraday's constant $23.06 \frac{kcal}{eV}$, and E_{ref} is the reference electrode potential for the ferrocenium electrode, calculated to be $4.988\ V$ in acetonitrile.[25]

This method predicts the quinone reduction potential under Ar quite well. However, as experimentally observed, the reduction potential becomes less negative as the CO_2 concentration in solution increases, meaning E_{red} is a function of CO_2 concentration. As a result, we postulate that the reduction process occurs concertedly with CO_2 binding, which is rational considering the activation energy of binding CO_2 is extremely small for doubly-reduced quinones, and in many cases reported to be < 10 kcal/mol. This reactive reduction requires a slight modification to the ΔG_{red} calculation which is necessary to incorporate the effects of CO_2 binding into the reduction potential scheme. For reduction potentials under CO_2, ΔG_{red} was computed using the following equation:

$$\Delta G_{red} = G_{QCO_2^{2-}} - (G_{Q^-} + G_{CO_2})$$

To ensure the reliability of our computational methods, we calculated the reduction potentials and CO_2 binding energies via a combination of methods composed of two density functionals – MN15 and *ω*-B97xD – and two basis sets – 6-311+G(d,p) and Def2-TZVP. The results of the four methods are summarized in the tables below.

We found virtually no difference in basis sets with the Minnesota 15 functional on either calculated property. However, the *ω*-B97xD functional predicted systematically less favorable CO_2 binding compared to MN15, but also more negative reduction potentials.

The method with the most accurate binding energies relative to experiment was *ω*-B97xD/Def2-TZVP (MAE = 1.24 kcal/mol). This method was also the least accurate in predicting experimental E_{red} value (MAE = 0.50 V). On the other hand, the MN15/6-311+G(d,p) method was most accurate for predicting

experimental Ered values (MAE = 0.14 V), but also had a relatively high MAE (4.80 kcal/mol) relative to experimental CO_2 binding energies.

ω-B97xD/Def2-TZVP excels in predicting binding free energies because it captures dispersion and electrostatic interactions quite well in all cases. However, it perhaps lacks sufficient accuracy in describing the electronic environment of anionic organic species, which tends to be a struggle for various density functionals. On the other hand, MN15/6-311+G(d,p) predicted much better reduction potentials possibly because it is highly parametrized for a wide range of organic species. Due to these observations, we report in the MS the predicted E_{red} values calculated via the MN15/6-311+G(d,p) method, whereas binding free energies are reported via ω-B97xD/Def2-TZVP.

Table S10.2. Summary of DFT calculated properties for molecules 1, 2, 4, and 5 using MN15/6-311+G(d,p). The reduction potentials under Ar, 5% CO_2, 30% CO_2, and 100% CO_2 are reported in V vs Fc/Fc^+. The binding free energy is reported in kcal/mol.

Molecule	**MN15/6-311+G(d,p)**				
	$E_{red,Ar}$	$E_{red,5\%CO2}$	$E_{red,30\%CO2}$	$E_{red,100\%CO2}$	$\Delta G_{binding}$
1	-2.05	-1.55	-1.50	-1.47	-10.1
2	-2.09	-1.61	-1.56	-1.53	-9.8
4	-2.02	-1.52	-1.47	-1.44	-10.0
5	-2.08	-1.61	-1.56	-1.53	-9.4

Table S10.3. Summary of DFT calculated properties for molecules 1, 2, 4, and 5 using MN15/Def2-TZVP. The reduction potentials under Ar, 5% CO_2, 30% CO_2, and 100% CO_2 are reported in V vs Fc/Fc^+. The binding free energy is reported in kcal/mol.

Molecule	**MN15/Def2-TZVP**				
	$E_{red,Ar}$	$E_{red,5\%CO2}$	$E_{red,30\%CO2}$	$E_{red,100\%CO2}$	$\Delta G_{binding}$
1	-2.12	-1.66	-1.62	-1.59	-9.1
2	-2.20	-1.67	-1.63	-1.60	-10.6
4	-2.11	-1.57	-1.52	-1.49	-11.1
5	-2.18	-1.67	-1.62	-1.59	-10.2

Table S10.4. Summary of DFT calculated properties for molecules 1, 2, 4, and 5 using ω-B97xD/6-311+G(d,p). The reduction potentials under Ar, 5% CO_2, 30% CO_2, and 100% CO_2 are reported in V vs Fc/Fc^+. The binding free energy is reported in kcal/mol.

Molecule	wB97xD/6-311+G(d,p)				
	$E_{red,Ar}$	$E_{red,5\%CO2}$	$E_{red,30\%CO2}$	$E_{red,100\%CO2}$	$\Delta G_{binding}$
1	-2.16	-1.74	-1.70	-1.66	-8.3
2	-2.03	-1.74	-1.69	-1.66	-5.2
4	-2.12	-1.70	-1.66	-1.63	-8.2
5	-2.17	-1.79	-1.74	-1.71	-7.3

Table S10.5. Summary of DFT calculated properties for molecules 1, 2, 4, and 5 using ω-B97xD/Def2-TZVP. The reduction potentials under Ar, 5% CO_2, 30% CO_2, and 100% CO_2 are reported in V vs Fc/Fc^+. The binding free energy is reported in kcal/mol.

Molecule	wB97xD/Def2-TZVP				
	$E_{red,Ar}$	$E_{red,5\%CO2}$	$E_{red,30\%CO2}$	$E_{red,100\%CO2}$	$\Delta G_{binding}$
1	-2.27	-1.99	-1.94	-1.91	-4.9
2	-2.19	-1.96	-1.91	-1.88	-3.9
4	-2.24	-1.83	-1.78	-1.75	-7.9
5	-2.30	-1.94	-1.90	-1.87	-6.7

Electronic structures and charge densities S11

The charge and spin densities of species **1**, **2**, **4**, and **5**, including their reduced forms, were calculated using Natural Bond Orbital (NBO) analysis.[26-27] This method was chosen over alternatives such as Mulliken and Atomic Polar Tensor (APT) population analyses due to its improved chemical interpretability and reduced sensitivity to basis set effects. NBO provides a more physically meaningful partitioning of electron density, offering insights into bonding interactions and charge localization that are often obscured or misrepresented by Mulliken or APT methods.

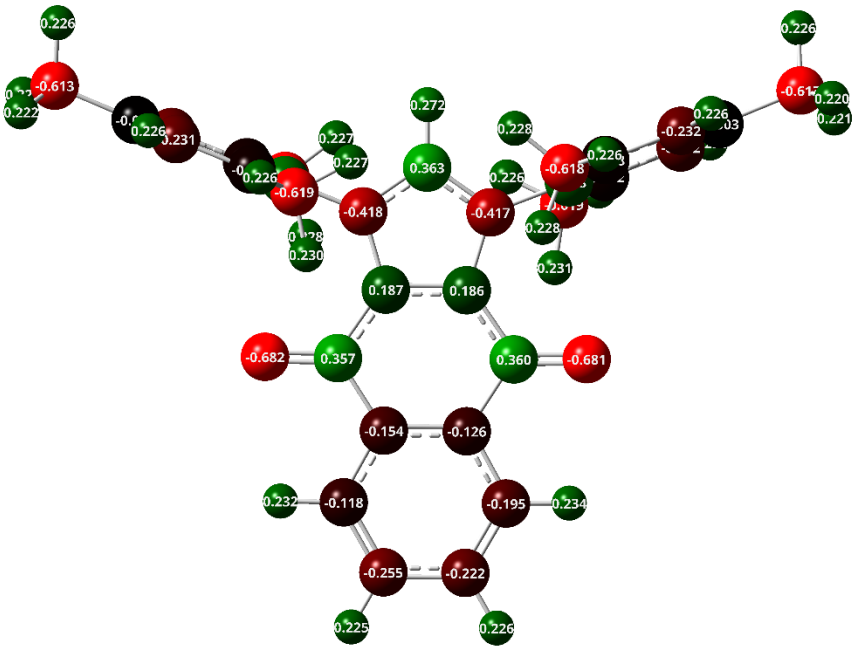

Figure S11.1. NBO charge density of singly reduced species **1**.

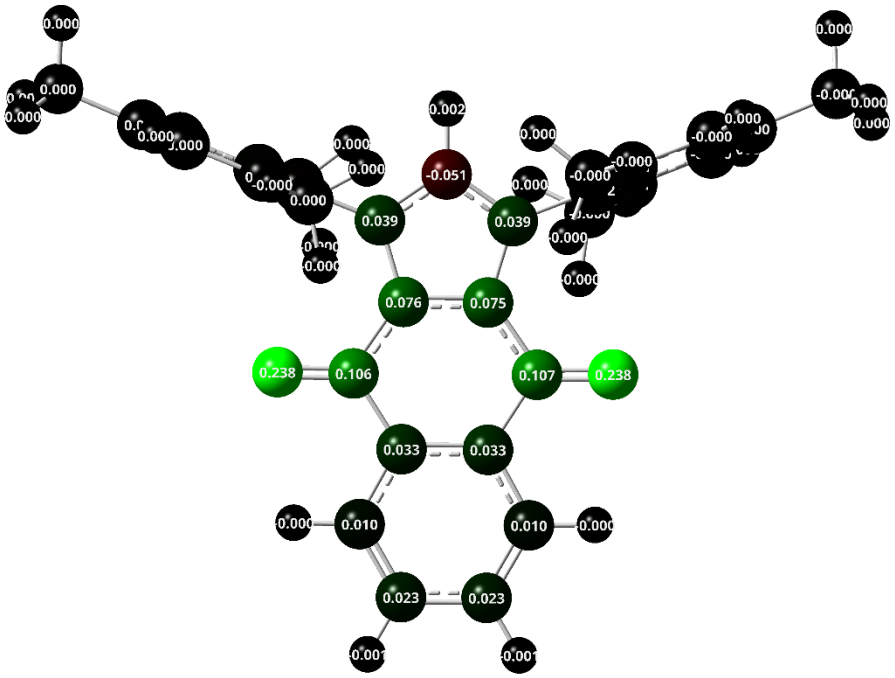

Figure S11.2. NBO spin density of singly reduced species **1**.

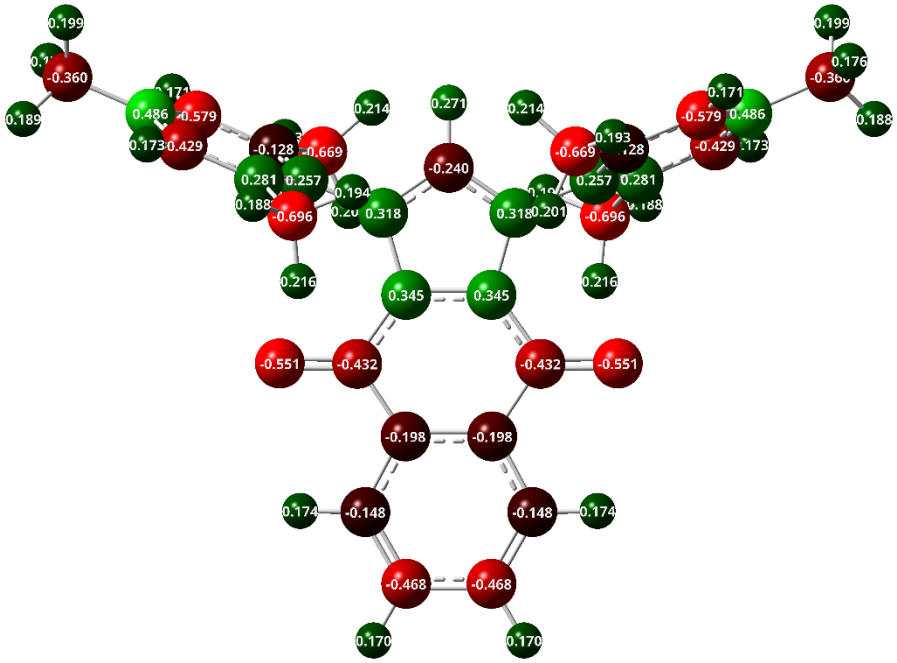

Figure S11.3. NBO charge density of doubly reduced species **1**.

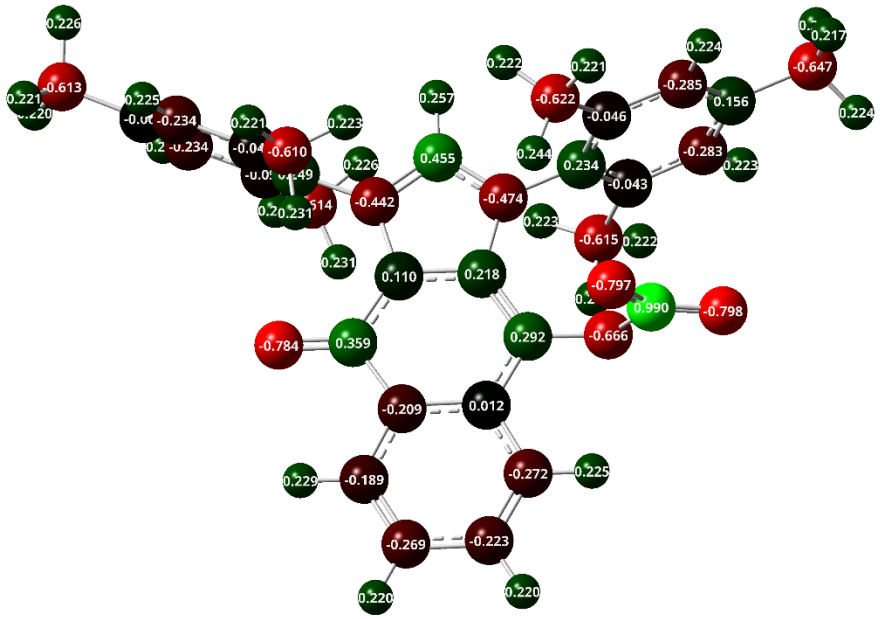

Figure S11.4. NBO charge density of doubly reduced species **1** with CO_2 bound.

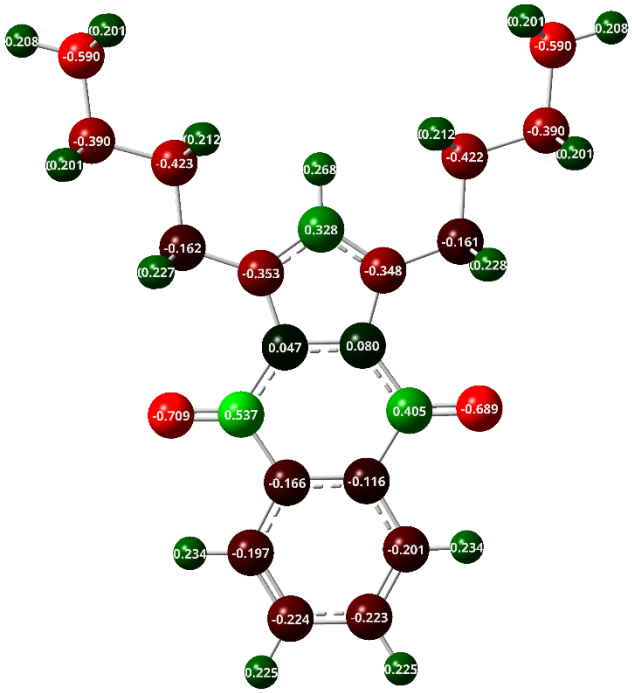

Figure S11.5. NBO charge density of singly reduced species **2**.

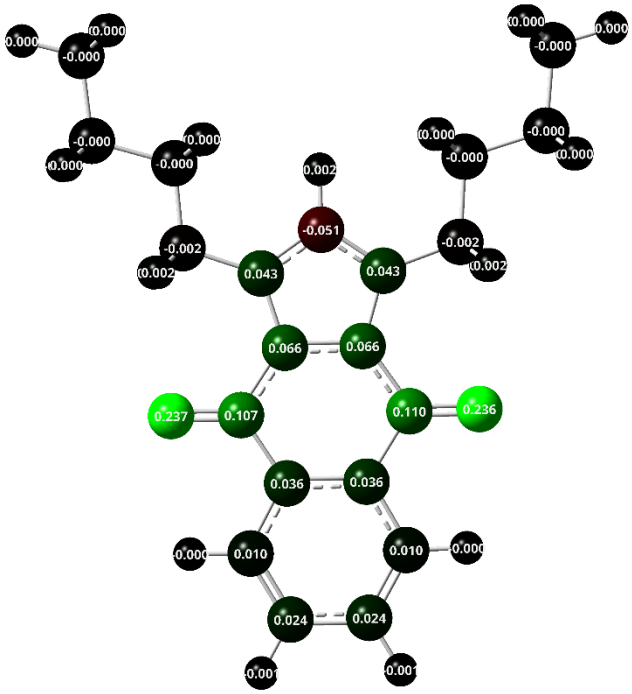

Figure S11.6. NBO spin density of singly reduced species **2**.

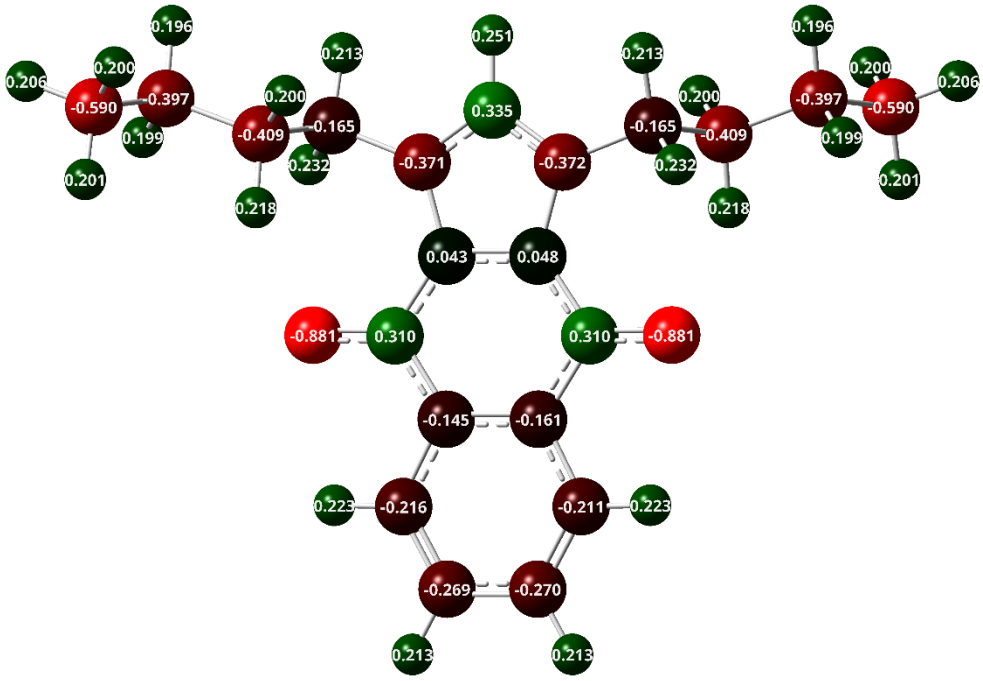

Figure S11.7. NBO charge density of doubly reduced species **2**.

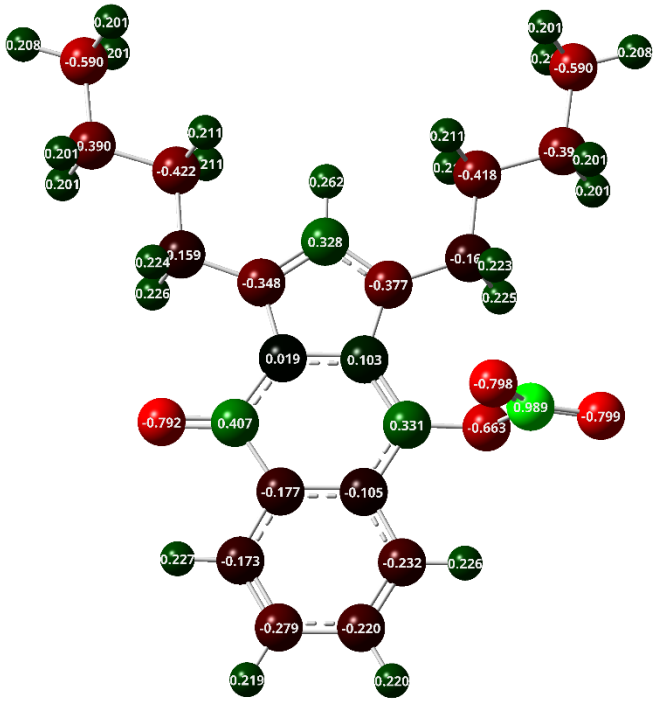

Figure S11.8. NBO charge density of doubly reduced species **2** with CO_2 bound.

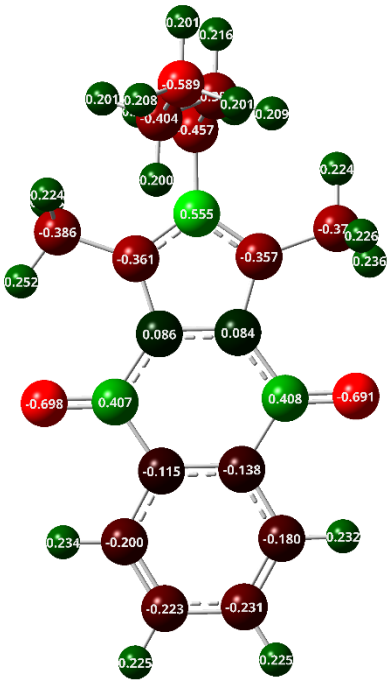

Figure S11.9. NBO charge density of singly reduced species **4**.

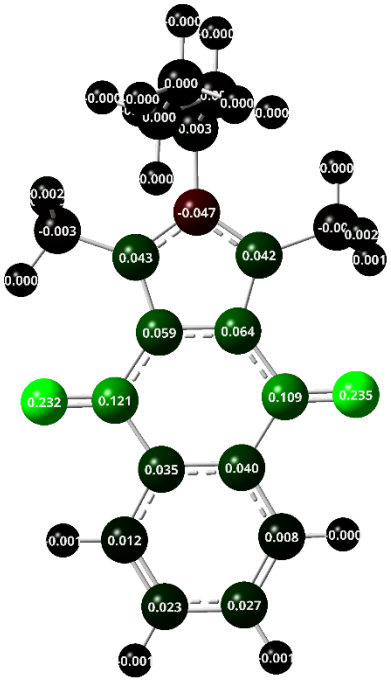

Figure S11.10. NBO spin density of singly reduced species **4**.

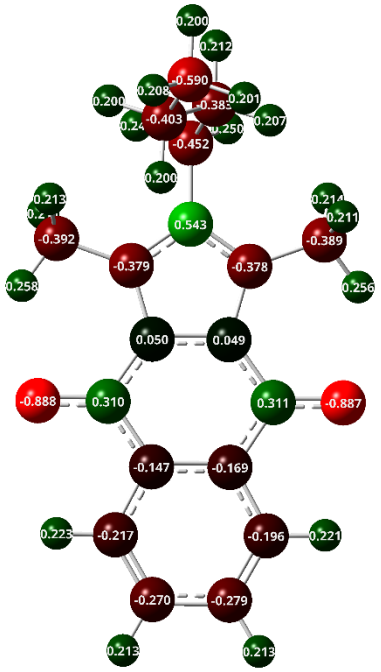

Figure S11.11. NBO charge density of doubly reduced species **4**.

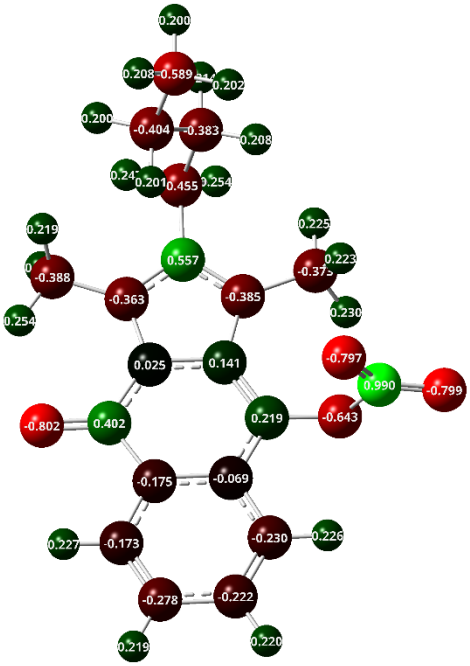

Figure S11.12. NBO charge density of doubly reduced species **4** with CO_2 bound.

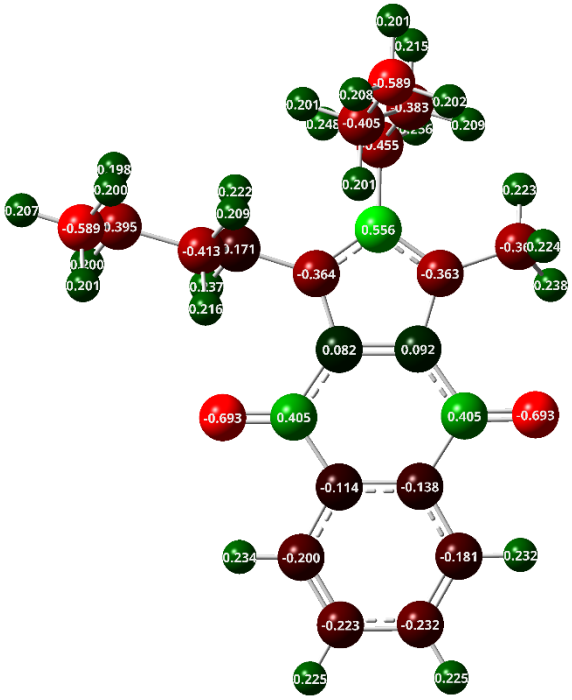

Figure S11.13. NBO charge density of singly reduced species **5**.

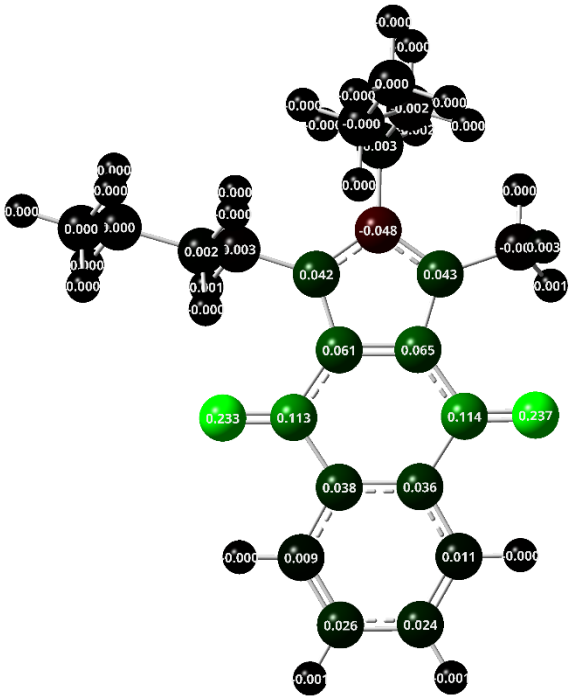

Figure S11.14. NBO spin density of singly reduced species **5**.

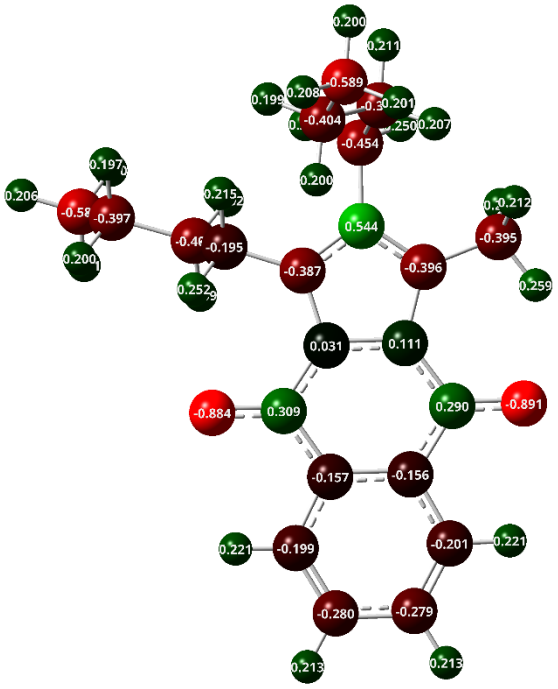

Figure S11.15. NBO charge density of doubly reduced species **5**.

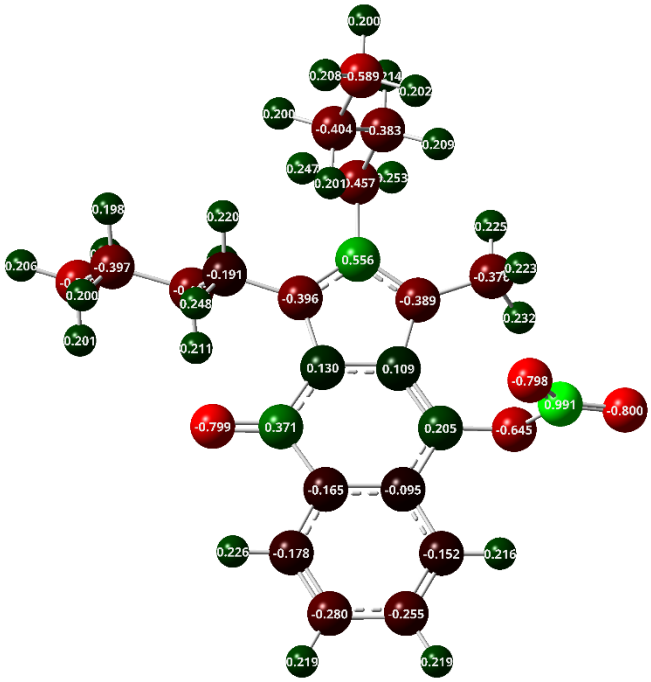

Figure S11.16. NBO charge density of doubly reduced species **5** with CO_2 bound.

1. Alherz, A. W.; Petersen, H. A.; Singstock, N. R.; Sur, S. N.; Musgrave, C. B.; Luca, O. R., Predictive energetic tuning of quinoid O-nucleophiles for the electrochemical capture of carbon dioxide. *Energy Advances* **2022,** *1* (11), 900-907.
2. Lee, J.; Kim, H.; Park, M. J., Long-Life, High-Rate Lithium-Organic Batteries Based on Naphthoquinone Derivatives. *Chemistry of Materials* **2016,** *28* (7), 2408-2416.
3. Mebrouk, K.; Camerel, F.; Jeannin, O.; Heinrich, B.; Donnio, B.; Fourmigué, M., High Photothermal Activity within Neutral Nickel Dithiolene Complexes Derived from Imidazolium-Based Ionic Liquids. *Inorganic Chemistry* **2016,** *55* (3), 1296-1303.
4. Yuan, J.; Liu, Z.; Dong, Y.; Gao, F.; Xia, X.; Wang, P.; Luo, Y.; Zhang, Z.; Yan, D.; Zhang, W., Pioneering 4,11-Dioxo-4,11-dihydro-1H-anthra[2,3-d]imidazol-3-ium Compounds as Promising Survivin Inhibitors by Targeting ILF3/NF110 for Cancer Therapy. *Journal of Medicinal Chemistry* **2023,** *66* (24), 16843-16868.
5. Liu, Z.; Zhang, Z.; Zhang, W.; Yan, D., 2-Substituted-1-(2-morpholinoethyl)-1 H -naphtho[2,3- d]imidazole-4,9-diones: Design, synthesis and antiproliferative activity. *Bioorganic & Medicinal Chemistry Letters* **2018,** *28* (14), 2454-2458.
6. Bruker-AXS *APEX4 V2022.1-1*, Bruker-AXS: Madison, WI, USA, 2022.
7. Sheldrick, G. M. *CELL_NOW*, Georg-August-Universität: Göttingen, Germany, 2008.
8. Sheldrick, G. M. *TWINABS* Bruker, Madison, Wisconsin, USA., 2012.
9. Sheldrick, G., SHELXT - Integrated space-group and crystal-structure determination. *Acta Crystallographica Section A* **2015,** *71* (1), 3-8.
10. Sheldrick, G., Crystal structure refinement with SHELXL. *Acta Crystallographica Section C* **2015,** *71* (1), 3-8.
11. Hubschle, C. B.; Sheldrick, G. M.; Dittrich, B., ShelXle: a Qt graphical user interface for SHELXL. *Journal of Applied Crystallography* **2011,** *44* (6), 1281-1284.
12. Jeffrey, G. A., *An introduction to hydrogen bonding*. Oxford University Press: 1997.
13. Frisch, M. J.; Trucks, G. W.; Schlegel, H. B.; Scuseria, G. E.; Robb, M. A.; Cheeseman, J. R.; Scalmani, G.; Barone, V.; Petersson, G. A.; Nakatsuji, H.; Li, X.; Caricato, M.; Marenich, A. V.; Bloino, J.; Janesko, B. G.; Gomperts, R.; Mennucci, B.; Hratchian, H. P.; Ortiz, J. V.; Izmaylov, A. F.; Sonnenberg, J. L.; Williams; Ding, F.; Lipparini, F.; Egidi, F.; Goings, J.; Peng, B.; Petrone, A.; Henderson, T.; Ranasinghe, D.; Zakrzewski, V. G.; Gao, J.; Rega, N.; Zheng, G.; Liang, W.; Hada, M.; Ehara, M.; Toyota, K.; Fukuda, R.; Hasegawa, J.; Ishida, M.; Nakajima, T.; Honda, Y.; Kitao, O.; Nakai, H.; Vreven, T.; Throssell, K.; Montgomery Jr., J. A.; Peralta, J. E.; Ogliaro, F.; Bearpark, M. J.; Heyd, J. J.; Brothers, E. N.; Kudin, K. N.; Staroverov, V. N.; Keith, T. A.; Kobayashi, R.; Normand, J.; Raghavachari, K.; Rendell, A. P.; Burant, J. C.; Iyengar, S. S.; Tomasi, J.; Cossi, M.; Millam, J. M.; Klene, M.; Adamo, C.; Cammi, R.; Ochterski, J. W.; Martin, R. L.; Morokuma, K.; Farkas, O.; Foresman, J. B.; Fox, D. J. *Gaussian 16 Rev. C.01*, Wallingford, CT, 2016.
14. Yu, H. S.; He, X.; Li, S. L.; Truhlar, D. G., MN15: A Kohn–Sham global-hybrid exchange–correlation density functional with broad accuracy for multi-reference and single-reference systems and noncovalent interactions. *Chemical Science* **2016,** *7* (8), 5032-5051.
15. Chai, J.-D.; Head-Gordon, M., Long-range corrected hybrid density functionals with damped atom–atom dispersion corrections. *Physical Chemistry Chemical Physics* **2008,** *10* (44), 6615.
16. McLean, A. D.; Chandler, G. S., Contracted Gaussian basis sets for molecular calculations. I. Second row atoms, *Z*=11–18. *The Journal of Chemical Physics* **1980,** *72* (10), 5639-5648.
17. Krishnan, R.; Binkley, J. S.; Seeger, R.; Pople, J. A., Self-consistent molecular orbital methods. XX. A basis set for correlated wave functions. *The Journal of Chemical Physics* **1980,** *72* (1), 650-654.
18. Weigend, F.; Ahlrichs, R., Balanced basis sets of split valence, triple zeta valence and quadruple zeta valence quality for H to Rn: Design and assessment of accuracy. *Physical Chemistry Chemical Physics* **2005,** *7* (18), 3297.
19. Weigend, F., Accurate Coulomb-fitting basis sets for H to Rn. *Physical Chemistry Chemical Physics* **2006,** *8* (9), 1057.

20. Clark, T.; Chandrasekhar, J.; Spitznagel, G. W.; Schleyer, P. V. R., Efficient diffuse function-augmented basis sets for anion calculations. III. The 3-21+G basis set for first-row elements, Li–F. *Journal of Computational Chemistry* **1983,** *4* (3), 294-301.
21. Frisch, M. J.; Pople, J. A.; Binkley, J. S., Self-consistent molecular orbital methods 25. Supplementary functions for Gaussian basis sets. *The Journal of Chemical Physics* **1984,** *80* (7), 3265-3269.
22. Petersson, G. A.; Bennett, A.; Tensfeldt, T. G.; Al-Laham, M. A.; Shirley, W. A.; Mantzaris, J., A complete basis set model chemistry. I. The total energies of closed-shell atoms and hydrides of the first-row elements. *The Journal of Chemical Physics* **1988,** *89* (4), 2193-2218.
23. Petersson, G. A.; Al-Laham, M. A., A complete basis set model chemistry. II. Open-shell systems and the total energies of the first-row atoms. *The Journal of Chemical Physics* **1991,** *94* (9), 6081-6090.
24. Marenich, A. V.; Cramer, C. J.; Truhlar, D. G., Universal Solvation Model Based on Solute Electron Density and on a Continuum Model of the Solvent Defined by the Bulk Dielectric Constant and Atomic Surface Tensions. *The Journal of Physical Chemistry B* **2009,** *113* (18), 6378-6396.
25. Namazian, M.; Lin, C. Y.; Coote, M. L., Benchmark Calculations of Absolute Reduction Potential of Ferricinium/Ferrocene Couple in Nonaqueous Solutions. *Journal of Chemical Theory and Computation* **2010,** *6* (9), 2721-2725.
26. Foster, J. P.; Weinhold, F., Natural hybrid orbitals. *Journal of the American Chemical Society* **1980,** *102* (24), 7211-7218.
27. Reed, A. E.; Curtiss, L. A.; Weinhold, F., Intermolecular interactions from a natural bond orbital, donor-acceptor viewpoint. *Chemical Reviews* **1988,** *88* (6), 899-926.